MNRAS 000, 1–15 (2022) Preprint 29 August 2022 Compiled using MNRAS LATEX style file v3.0

No Evidence of a Correlation between Hα-to-UV Ratio and Burstiness for Typical Star-forming Galaxies at $z \sim 2$

Saeed Rezaee[1]★, Naveen A. Reddy[1], Michael W. Topping[2,3], Irene Shivaei[2,4], Alice E. Shapley[4], Tara Fetherolf[1], Mariska Kriek[5], Alison Coil[6], Bahram Mobasher[1], Brian Siana[1], Xinnan Du[7], Ali Ahmad Khostovan[8,9], Andrew Weldon[1], Najmeh Emami[10], and Nima Chartab[11]

[1]*Department of Physics and Astronomy, University of California, Riverside, CA 92521, USA*
[2]*Steward Observatory, University of Arizona, 933 North Cherry Avenue, Tucson, AZ 85721, USA*
[3]*Department of Physics and Astronomy, University of California, Los Angeles, CA 90095, USA*
[4]*Nasa Hubble fellow*
[5]*Astronomy Department, University of California, Berkeley, CA 94720, USA*
[6]*Center for Astrophysics and Space Sciences, Department of Physics, University of California, San Diego, 9500 Gilman Drive, La Jolla, CA 92093, USA*
[7] *Kavli Institute for Particle Astrophysics & Cosmology, P. O. Box 2450, Stanford University, Stanford, CA 94305, USA*
[8]*Astrophysics Division, NASA Goddard Space Flight Center, Greenbelt, MD 20771, USA*
[9]*NASA Postdoctoral Program Fellow*
[10]*Minnesota Institute for Astrophysics, University of Minnesota, 116 Church St SE, Minneapolis, MN 55455, USA*
[11]*The Observatories of the Carnegie Institution for Science, 813 Santa Barbara St., Pasadena, CA 91101, USA*

Accepted XXX. Received YYY; in original form ZZZ

ABSTRACT

It has long been uncertain how effective the dust-corrected Hα-to-UV luminosity ratio ($L(\mathrm{H}\alpha)/L(\mathrm{UV})$) is in probing bursty star-formation histories (SFHs) for high-redshift galaxies. To address this issue, we present a statistical analysis of the resolved distribution of star-formation-rate surface density (Σ_{SFR}) as well as stellar age and their correlations with the globally measured $L(\mathrm{H}\alpha)/L(\mathrm{UV})$ for a sample of 310 star-forming galaxies in two redshift bins of $1.37 < z < 1.70$ and $2.09 < z < 2.61$ observed by the MOSFIRE Deep Evolution Field (MOSDEF) survey. We use the multi-waveband CANDELS/3D-HST imaging of MOSDEF galaxies to construct Σ_{SFR} and stellar age maps. We also analyze the composite rest-frame far-UV spectra of a subsample of MOSDEF targets obtained by the Keck Low Resolution Imager and Spectrometer (LRIS), which includes 124 star-forming galaxies at redshifts $1.4 < z < 2.6$, to examine the average stellar population properties, and the strength of extremely age-sensitive FUV spectral features in bins of $L(\mathrm{H}\alpha)/L(\mathrm{UV})$. We find no evidence that galaxies with higher $L(\mathrm{H}\alpha)/L(\mathrm{UV})$ are undergoing a burst of star formation based on the distribution of Σ_{SFR} and stellar age as well as the strengths of Si IV $\lambda\lambda$1393, 1402 and C IV $\lambda\lambda$1548, 1550 P-Cygni features from massive stars. Our results suggest that the $L(\mathrm{H}\alpha)/L(\mathrm{UV})$ ratio is not a reliable tracer of bursty SFHs for typical star-forming galaxies at high redshift. We also study the variations observed in the strength of the nebular He II λ1640 emission between the $L(\mathrm{H}\alpha)/L(\mathrm{UV})$ subsamples. We find that variations in the upper-mass limit of the IMF cannot fully account for all the observed difference in the HeII emission between the $L(\mathrm{H}\alpha)/L(\mathrm{UV})$ subsamples, and that another source of He^+ ionizing photons, such as X-ray binaries, may be needed to explain such a difference.

Key words: galaxies: starbursts — galaxies: evolution — galaxies: high-redshift — galaxies: ISM — ISM: dust, extinction

1 INTRODUCTION

While most galaxies follow a tight sequence in star-formation rate (SFR) versus stellar mass (M_*), there are some that are significantly offset above this relation at any given redshift, suggestive of a recent burst of star formation (Schmidt 1959; Kennicutt 1989; Somerville & Primack 1999; Springel 2000; Springel et al. 2005; Noeske et al. 2007; Kereš et al. 2009; Knapen & James 2009; Dobbs & Pringle 2009; Genzel et al. 2010; Governato et al. 2010; Reddy et al. 2012; Rodighiero et al. 2014; Hopkins et al. 2014; Shivaei et al. 2015; Hayward & Hopkins 2017; Fujimoto et al. 2019). For example, the apparent increase in scatter of the relationship between SFR and M_* at low stellar masses suggests that such galaxies are characterized by bursty star-formation histories (Noeske et al. 2007; Hopkins et al. 2014; Asquith et al. 2018; Dickey et al. 2021; Atek et al. 2022). In addition, simulations with resolved scaling comparable to the star forming clouds suggest that the burst amplitude and frequency increases with redshift (e.g., Feldmann et al. 2017; Sparre et al. 2017; Ma et al. 2018). Given that bursty SFHs are inferred to be the likely mode of galaxy growth for at least lower mass galaxies at high-

★ E-mail: saeed.rezaee@email.ucr.edu

redshift (e.g., Atek et al. 2022 found evidence of bursty SFHs for lower mass galaxies with $M_* < 10^9\,M_\odot$ at $z \sim 1.1$), it is important to determine the effectiveness of commonly-used proxies for burstiness.

A key method that has been used to infer the burstiness of star-forming galaxies is to compare SFR indicators that are sensitive to star formation on different timescales. Two of the widely used SFR indicators are derived from the Hα nebular recombination line ($\lambda = 6564.60$ Å) and far-ultraviolet (FUV) continuum (1300 Å $< \lambda <$ 2000 Å). The Hα emission line originates from the recombination of the ionized gas around young massive stars ($M_* \gtrsim 20\,M_\odot$) and traces SFR over a timescales of ~ 10 Myr (Kennicutt & Evans 2012). The UV continuum is sensitive to the same stars that are responsible for Hα, as well as lower-mass stars (B stars, and A stars at wavelengths redder than 1700 A) with lifetimes of ~ 100 Myr and $M_* \gtrsim 3M_\odot$. As a result, when compared to the Hα emission line, the FUV continuum traces SFRs averaged over a longer timescale. Therefore, variations in the dust-corrected Hα-to-UV luminosity ratio ($L(\mathrm{H}\alpha)/L(\mathrm{UV})$) may reveal information about recent burst activity (Glazebrook et al. 1999; Iglesias-Páramo et al. 2004; Lee et al. 2009; Meurer et al. 2009; Hunter et al. 2010; Fumagalli et al. 2011; Lee et al. 2011; Weisz et al. 2012; da Silva et al. 2012, 2014; Domínguez et al. 2015; Emami et al. 2019; Caplar & Tacchella 2019; Faisst et al. 2019).

For a constant star-formation history (SFH), the Hα-to-UV luminosity ratio will reach to its equilibrium after a few tens of Myr (e.g., Reddy et al. 2012). However, variations in the inferred integrated Hα-to-UV ratio may result from a number of effects, including variations in the IMF (Leitherer & Heckman 1995; Elmegreen 2006; Pflamm-Altenburg et al. 2007; Meurer et al. 2009; Pflamm-Altenburg et al. 2009; Hoversten & Glazebrook 2008; Boselli et al. 2009; Mas-Ribas et al. 2016), nebular and stellar dust reddening (Kewley et al. 2002; Lee et al. 2009; Reddy et al. 2012; Reddy et al. 2015; Shivaei et al. 2015, 2018; Theios et al. 2019), ionizing escape fraction (Steidel et al. 2001; Shapley et al. 2006; Siana et al. 2007), and binary stellar evolution (Eldridge 2012; Eldridge et al. 2017; Choi et al. 2017). Given these possibilities, any interpretation about the burstiness of galaxies based on the variations in $L(\mathrm{H}\alpha)/L(\mathrm{UV})$ must be approached with caution.

The MOSFIRE Deep Evolution Field (MOSDEF) survey is ideally suited to examine the extent to which variations in $L(\mathrm{H}\alpha)/L(\mathrm{UV})$ trace burstiness. MOSDEF probes galaxies at $z \sim 2$, which marks a key epoch for galaxy growth when the cosmic star-formation density reaches its maximum (Madau et al. 1996; Hopkins & Beacom 2006; Madau & Dickinson 2014). Additionally, the deep Hubble Space Telescope (HST) imaging of the MOSDEF galaxies obtained by CANDELS (Grogin et al. 2011; Koekemoer et al. 2011) enables the construction of stellar population maps that can be used to assess burstiness on smaller (resolved) spatial scales (e.g., Wuyts et al. 2011, 2012; Hemmati et al. 2014; Jafariyazani et al. 2019; Fetherolf et al. 2020). Moreover, the availability of follow-up Keck/LRIS rest-FUV spectra of a subset of 259 MOSDEF galaxies (Topping et al. 2020; Reddy et al. 2022) allows us to investigate the relationship between the $L(\mathrm{H}\alpha)/L(\mathrm{UV})$ ratio and age-sensitive FUV spectral features.

The goal of this study is to determine whether the dust-corrected Hα-to-UV luminosity ratio is a reliable tracer of a bursty SFH at $z \sim 2$. We address this question by examining the correlations between the differences in properties of the stellar populations and the $L(\mathrm{H}\alpha)/L(\mathrm{UV})$ ratio. The structure of this paper is as follows. In Section 2, we introduce the samples used in this work, and outline the sample selection criteria and data reduction. In Section 3, we describe the method used for constructing the stellar population maps, and the result of the morphology analysis. Our approach for constructing rest-FUV composite spectra is described in Section 4. Our results on variations of the average physical properties of galaxies, and the strength of age-sensitive FUV spectral features in bins of $L(\mathrm{H}\alpha)/L(\mathrm{UV})$ are presented in Section 5. Finally, the conclusions are summarized in Section 6. Wavelengths are in the vacuum frame. We adopt a flat cosmology with $H_0 = 70\,\mathrm{km\,s^{-1}}$, $\Omega_\Lambda = 0.7$, and $\Omega_m = 0.3$. A Chabrier (2003) IMF is assumed throughout this work.

2 SAMPLE

2.1 Rest-Frame Optical MOSDEF Spectroscopy, CANDELS/3D-HST Imaging

The MOSDEF survey (Kriek et al. 2015) used the Keck/MOSFIRE spectrograph (McLean et al. 2012) to obtain rest-frame optical spectra of ~ 1500 H-band-selected star-forming galaxies and active galactic nuclei (AGNs). The five extragalactic legacy fields (GOODS-S, GOODS-N, COSMOS, UDS, AEGIS) covered by the CANDELS survey (Grogin et al. 2011; Koekemoer et al. 2011) were targeted. The targets were chosen to lie in three redshift bins: $1.37 < z < 1.70$, $2.09 < z < 2.61$, and $2.95 < z < 3.80$ where the strong rest-frame optical emission lines ([O II]λ3727, 3730, Hβ, [O III]$\lambda\lambda$4960, 5008, Hα, [N II]$\lambda\lambda$6550, 6585, and [S II]λ6718, 6733) are redshifted into the YJH, JHK, and HK transmission windows, respectively. Further details of the survey and MOSFIRE spectroscopic data reduction are provided in Kriek et al. (2015).

We use the spectroscopic redshifts and emission lines measured by the MOSDEF survey. The spectroscopic redshift for each target was measured from the observed wavelength centroid of the highest signal-to-noise emission line in each spectrum. Emission line fluxes were measured from the 1D-spectra of the individual objects by fitting Gaussian functions along with a linear continuum. The Hα was fit simultaneously with the [N II] doublet using three Gaussian functions. The Hα emission line flux was corrected for the underlying Balmer absorption, which was measured from the best-fit stellar population model (Section 2.3). Line flux uncertainties were calculated by perturbing the observed spectra according to their error spectra and remeasuring the line fluxes 1000 times. The 68th percentile of the distribution obtained from these iterations was adopted to represent the upper and lower flux uncertainties (e.g., Reddy et al. 2015; Freeman et al. 2017).

Resolved broad-band photometry of the MOSDEF galaxies was obtained by CANDELS using *HST*/ACS in the $F435W$ (B_{435}), $F606W$ (V_{606}), $F775W$ (i_{775}), $F813W$ (I_{814}), and $F850LP$ (z_{850}) filters and *HST*/WFC3 in the $F125W$ (J_{125}), $F140W$ (JH_{140}), and $F160W$ (H_{160}) filters. CANDELS imaging covered $\sim 960\,\mathrm{arcmin}^2$ up to a 90% completeness in the H_{160} filter at a magnitude of 25 mag. To construct stellar population maps for the sample galaxies, we use the processed CANDELS images provided by the 3D-HST grism survey team (Momcheva et al. 2016; Skelton et al. 2014; Brammer et al. 2012) along with the publicly available[1] photometric catalogs with coverage from 0.3 μm to 0.8 μm. The HST images provided by the 3D/HST team were drizzled to a 0.06 arcsec pixel^{-1} scale and smoothed to produce the same spatial resolution as the H_{160} images (0.18 arcsec).

The final sample used in this work contains 310 typical star-forming galaxies at $1.36 < z < 2.66$, all meeting the following criteria. They all have spectroscopic redshifts from the MOSDEF survey and detections of Hα and Hβ emission lines with $S/N \geqslant 3$. AGNs were identified and excluded from the sample based on the

[1] https://archive.stsci.edu/prepds/3d-hst/

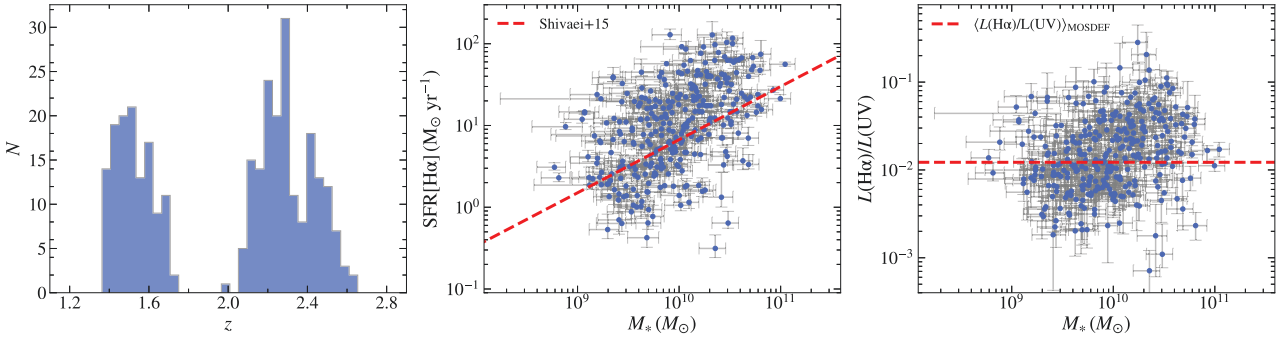

Figure 1. Physical properties of 310 star-forming galaxies in the MOSDEF/MORPH sample used in this work. *Left*: The histogram indicates the MOSDEF spectroscopic redshift distribution in two bins with the average redshifts of $z \sim 1.5$ and $z \sim 2.3$. *Middle*: SFR[Hα] vs. M_* relationship. SFR[Hα] is computed using the dust-corrected Hα luminosity. The conversion factor between the Hα luminosity and SFR[Hα], as well as stellar mass are derived using the SED modeling. The dashed red line shows Shivaei et al. (2015) relationship between SFR[Hα] and M_*, which has been adjusted to represent the assumptions used in this work, based on the first two years of MOSDEF (including galaxies with undetected Hβ). *Right*: The distribution of dust-corrected $L(\mathrm{H}\alpha)/L(\mathrm{UV})$ with respect to the stellar mass where $L(\mathrm{H}\alpha)$ and $L(\mathrm{UV})$ are dust-corrected using the Cardelli et al. (1989) and SMC extinction curves, respectively. The red line indicates the average dust-corrected $L(\mathrm{H}\alpha)/L(\mathrm{UV})$ of all the galaxies in the MOSDEF parent sample that have coverage of Hα and Hβ emission lines with $S/N \geqslant 3$.

IR properties, X-ray luminosities, or [N II]λ6584/Hα line ratio criteria as described in Coil et al. (2015), Azadi et al. (2017, 2018), and Leung et al. (2019). Additional S/N and resolution constraints were applied to the HST photometry as a result of our approach of grouping pixels which will be discussed in Section 3.

The final sample described above is used to analyze the morphological information of the MOSDEF galaxies in the first part of this work (i.e., Section 3), and is referred to as the MOSDEF/MORPH sample throughout this work. This sample is based on that used by Fetherolf et al. (2022, submitted). The MOSDEF/MORPH sample covers a range of stellar mass of $8.77 < \log[M_*/M_\odot] < 11.04$, and a SFR[H$\alpha$] range of $0.40 < (\mathrm{SFR}[\mathrm{H}\alpha]/M_\odot \mathrm{yr}^{-1}) < 130$. As shown in the middle panel of Figure 1, the MOSDEF/MORPH sample galaxies lie systematically above the mean main-sequence relation found by Shivaei et al. (2015) based on the first two years of MOSDEF. This is due to the S/N and resolution criteria (Section 3) imposed on the HST photometry of MOSDEF galaxies. Using these requirements results in a sample that is biased against low-mass and compact galaxies (Fetherolf et al. 2020). The MOSDEF/MORPH sample galaxies exhibit a similar range of $L(\mathrm{H}\alpha)/L(\mathrm{UV})$ to the MOSDEF parent sample galaxies that have coverage of Hα and Hβ with significant detections ($S/N \geqslant 3$) and include galaxies with $L(\mathrm{H}\alpha)/L(\mathrm{UV})$ that lie at least 5σ below the mean ratio for the MOSDEF parent sample. As mentioned earlier in this section, $L(\mathrm{H}\alpha)$ used here is obtained by the MOSDEF survey, and is corrected for the effect of dust using a MW extinction curve (Cardelli et al. 1989) which is shown to best represent the nebular attenuation curve for both high-redshift and local galaxies (Reddy et al. 2020; Rezaee et al. 2021). UV luminosity ($L(\mathrm{UV})$) is estimated from the best-fit SED model (Section 2.3) at $\lambda = 1500$ Å. We correct $L(\mathrm{UV})$ for dust using the SMC extinction curve (Fitzpatrick & Massa 1990; Gordon et al. 2003) and SED-based continuum reddening ($E(B-V)_{\mathrm{cont}}$).

2.2 MOSDEF/LRIS Rest-FUV Spectroscopy

A subset of 259 objects from the MOSDEF parent sample were selected for deep rest-FUV spectroscopic follow-up observations with the Keck I/Low Resolution Imager and Spectrometer (LRIS; Oke et al. 1995; Steidel et al. 2004). We refer the reader to Topping et al. (2020) and Reddy et al. (2022) for further details about the MOSDEF/LRIS survey data collection and reduction procedures. In brief, targets were prioritized based on $S/N \geqslant 3$ detection of the four emission lines ([O III], Hβ, [N II]λ6584, and Hα) measured by the MOSDEF survey. Objects with available Hα, Hβ, and [O III] as well as an upper limit on [N II] were accorded the next highest priority. The objects with available spectroscopic redshifts from the MOSDEF survey, as well as those without a secure redshift measurements, were also included. The lowest priority was assigned to the objects that were not included in the MOSDEF survey, but had photometric redshifts and apparent magnitudes from the 3D-HST catalogs that were within the MOSDEF survey redshift ranges.

Rest-FUV LRIS spectra were obtained within 9 multi-object slit masks with 1.″2 slits in four extragalactic legacy fields: GOODS-S, GOODS-N, AEGIS, COSMOS. The d500 dichroic was used to split the incoming beam at ≃ 5000 Å were used to obtain the LRIS spectra. The blue and red-side channels of LRIS were observed with the 400 line/mm grism blazed at 4300 Å, and the 600 line/mm grating blazed at 5000 Å, respectively. This configuration yielded a continuous wavelength range from the atmospheric cutoff at 3100 Å to ∼ 7650 Å (the red wavelength cutoff depends on the location of the slit in the spectroscopic field of view) with a resolution of $R \sim 800$ on the blue side and $R \sim 1300$ on the red side. The final MOSDEF/LRIS sample used in the second part of this work (i.e., Section 5) includes 124 star-forming galaxies at $1.42 < z < 2.58$, all meeting the same S/N and redshift measurement requirements as those mentioned in Section 2.1.

2.3 SED Modeling

We use the Binary Population and Spectral Synthesis (BPASS) version 2.2.1 models[2] (Eldridge et al. 2017; Stanway & Eldridge 2018) to infer UV luminosity ($L(\mathrm{UV})$), stellar continuum reddening ($E(B-V)_{\mathrm{cont}}$), stellar ages, conversion factors between luminosities and SFRs, as well as stellar masses (M_*). The effect of binary stellar evolution is included in the BPASS SED models, which has been found to be an important assumption in modeling the spectra of high redshift galaxies (Steidel et al. 2016; Eldridge et al. 2017;

[2] https://bpass.auckland.ac.nz/

Reddy et al. 2022). These models are characterized by three sets of parameters, stellar metallicity (Z_*) ranging from 10^{-5} to 0.040 in terms of mass fraction of metals where solar metallicity ($Z_\odot$) is equal to 0.0142 (Asplund et al. 2009), the upper-mass cutoff of the IMF ($M_{\rm cutoff}$ = $\{100M_\odot, 300M_\odot\}$), and the choice of including binary stellar evolution. These parameters divide the models into four sets of model assumptions with various $M_{\rm cutoff}$ and whether or not the binary effects are included. Throughout, we refer to these model combinations as "100bin", "300bin", "100sin", and "300sin" where the initial number indicate the $M_{\rm cutoff}$ of the IMF and "bin" ("sin") indicates that the binary evolution is (or is not) included (Reddy et al. 2022).

Stellar population synthesis (SPS) models are constructed by adding the original instantaneous-burst BPASS models for ages ranging from 10^7 -10^{10} yr while adopting a constat star-formation history. The choice of constant SFH over instantaneous burst models is based on the fact that the latter are better suited for the individual massive star clusters that are more age-sensitive than the entire high-redshift star-forming galaxies, which have dynamical times that are typically far greater than a few Myr (Shapley et al. 2001; Papovich et al. 2001; Reddy et al. 2012). The reddening of the stellar continuum is added to the models assuming the following attenuation curves: the SMC (Gordon et al. 2003), Reddy et al. (2015), and Calzetti et al. (2000), with stellar continuum reddening in range of $E(B-V)_{\rm cont} = 0.0 - 0.60$. Based on earlier studies, these curves are shown to best represent the shape of the dust attenuation curves for the majority of high-redshift galaxies (e.g., Reddy et al. 2018; Fudamoto et al. 2020; Shivaei et al. 2020).

When fitting the broadband photometry, the stellar metallicity is held fixed at $\langle Z_* \rangle = 0.001$ as this value was found to best fit the rest-FUV spectra of galaxies in the MOSDEF/LRIS sample (Topping et al. 2020; Reddy et al. 2022). The stellar population ages of the models are permitted to range between $\sim$ 10 Myr and the age of the universe at the redshift of each galaxy. Unless mentioned otherwise, the BPASS model with binary stellar evolution, an upper-mass cutoff of 100 $M_\odot$ ("100bin"), and the SMC extinction curve are adopted for this analysis. Previous studies (e.g., Reddy et al. 2022) have shown that using the SMC dust attenuation curve results in better agreement between Hα and SED derived SFRs. Assuming the Z_* = 0.001 100bin BPASS SPS models in fitting the broadband photometry yields a conversion factor of 2.12×10^{-42} $M_\odot {\rm yr}^{-1} {\rm erg}^{-1}$s between the dust-corrected Hα luminosity and SFR[Hα].

The best-fit SED model is chosen by fitting the aforementioned models to the broadband photometry. The parameters of the model with the lowest χ^2 relative to the photometry are considered to be the best-fit values. The errors in the parameters are calculated by fitting the models to many perturbed realizations of the photometry according to the photometric errors. The resulting standard deviations in the best-fit model values give the uncertainties in these values.

3 MORPHOLOGY ANALYSIS

In this section we present a methodology to construct resolved stellar population maps that may unveil galaxies undergoing bursts of star formation on smaller ($\sim$10 kpc) spatial scales. We also examine the correlation between the resolved stellar population properties and L(Hα)/L(UV).

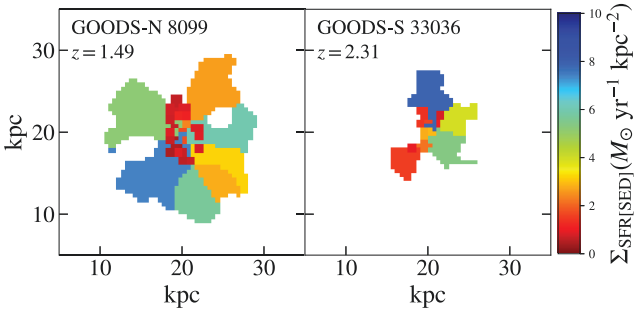

Figure 2. Examples of star-formation-rate surface density ($\Sigma_{\rm SFR[SED]}$) maps using Voronoi bins. The field name and 3D-HST Version 4.0 ID of each galaxy, as well as their redshifts, are indicated in the top left corner of each panel.

3.1 Pixel Binning

Rather than studying the individual images pixel by pixel, we group pixels using the two-dimensional Voronoi binning technique introduced by Cappellari & Copin (2003) and further modified by Fetherolf et al. (2020). The point spread function of the CANDELS imaging is larger than the individual pixels (0.″18), such that we apply a Voronoi binning technique to the imaging in order to avoid correlated noise between individual analyzed elements. In brief, each of the 3D-HST images (Section 2.1) is divided into sub-images 80 pixels on a side. We use the SExtractor (Bertin, E. & Arnouts, S. 1996) segmentation map to mask pixels in each sub-image that are not associated with the galaxy. The pixels are grouped following the algorithm presented in Cappellari & Copin (2003) to attain $S/N \geqslant 5$ in at least five different filters (e.g., see Fetherolf et al. 2020). Alongside CANDELS imaging, we use unresolved *Spitzer*/IRAC photometry to cover the rest-frame near-infrared part of the spectrum. As the HST and Spitzer/IRAC photometry have different spatial resolutions, we assign IRAC fluxes to each of the Voronoi bins proportionally according to the H_{160} flux (see Fetherolf et al. 2020 for further details). The stellar population properties for each Voronoi bin are inferred using the SED models (see Section 2.3) that best fit the resolved 3D-HST photometry. We calculate star-formation-rate surface density ($\Sigma_{\rm SFR[SED]}$) for each Voronoi bin by dividing the SFR determined from the best-fit resolved SED model by the area of each Voronoi bin. Figure 2 shows examples of the Voronoi bins and stellar population maps for two galaxies in the sample, one in each targeted redshift range.

3.2 Patchiness

Patchiness (P) is a recently introduced morphology metric (Fetherolf et al. 2022) that evaluates the Gaussian likelihood that each of the distinct components of a distribution are equal to the weighted average of the distribution. In this analysis, individual elements are values of a parameter measured for each of the resolved Voronoi bins. The area-weighted average of the parameter X measured from individual Voronoi bins is defined by

$$\langle X \rangle = \frac{\sum_{i=1}^{N_{\rm bins}} n_{{\rm pix},i} X_i}{\sum_{i=1}^{N_{\rm bins}} n_{{\rm pix},i}}, \quad (1)$$

where X_i are the values measured for the parameter X inside each of the Voronoi bins with uncertainty σ_i, $N_{\rm bins}$ is the total number of Vornoi bins in a galaxy photometry, and $n_{\rm pix}$ is the total number of

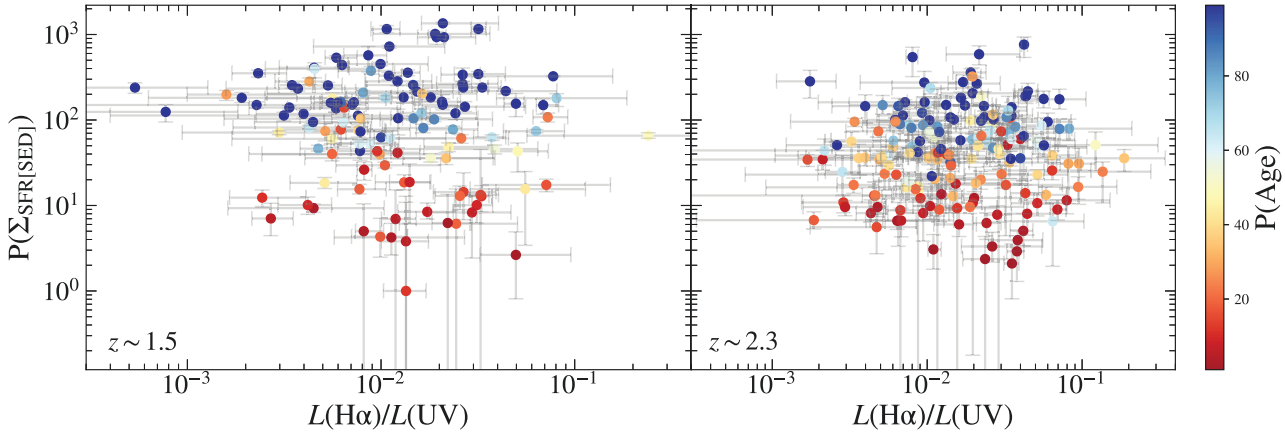

Figure 3. The MOSDEF/MORPH sample: $P(\Sigma_{\mathrm{SFR[SED]}})$ versus dust-corrected $L(\mathrm{H}\alpha)/L(\mathrm{UV})$ for two redshift bins centered at $z \sim 1.5$ (*left*) and $z \sim 2.3$ (*right*). The points are colored by patchiness of the stellar age. No significant correlations is found between $L(\mathrm{H}\alpha)/L(\mathrm{UV})$ and $P(\Sigma_{\mathrm{SFR[SED]}})$, or between $L(\mathrm{H}\alpha)/L(\mathrm{UV})$ and $P(\mathrm{Age})$. The Spearman correlation properties for the relations shown in this figure are reported in Table 1.

Table 1. Results of Spearman correlation tests between $L(\mathrm{H}\alpha)/L(\mathrm{UV})$ and $P(\mathrm{Age})$, as well as $L(\mathrm{H}\alpha)/L(\mathrm{UV})$ and $P(\Sigma_{\mathrm{SFR[SED]}})$.

Redshift bins		p-value[a]	P_s[b]
$z \sim 1.5$	$P(\mathrm{Age})$[c]	-0.04	0.62
	$P(\Sigma_{\mathrm{SFR[SED]}})$[d]	-0.09	0.30
$z \sim 2.3$	$P(\mathrm{Age})$	0.06	0.43
	$P(\Sigma_{\mathrm{SFR[SED]}})$	0.07	0.36

[a] The Spearman correlation coefficient between $L(\mathrm{H}\alpha)/L(\mathrm{UV})$ and each of the listed parameters using the MOSDEF/MORPH sample.
[b] The probability of null correlation between $L(\mathrm{H}\alpha)/L(\mathrm{UV})$ and each of the listed parameters using the MOSDEF/MORPH sample.
[c] Patchiness of the stellar population age.
[d] Patchiness of the star-formation-rate surface density.

pixels inside a single Voronoi bin (area). The patchiness, $P(X)$, can be calculate by Equation 2 in Fetherolf et al. 2022 as:

$$P(X) = -\ln\left\{\prod_{i=1}^{N_{bins}} \frac{1}{\sqrt{2\pi}\sigma_i} \exp\left[-\frac{(X_i - \langle X\rangle)^2}{2\sigma_i^2}\right]\right\}. \quad (2)$$

A detailed discussion of the patchiness metric properties is presented in Fetherolf et al. 2022. In brief, patchiness can be compared most reliably between galaxies with similar redshifts. Thus, we divide galaxies into two bins of redshift and analyze the patchiness separately for galaxies in each bin. Moreover, patchiness can be used on parameters with large dynamic range or parameters with values close to zero. We study patchiness of $\Sigma_{\mathrm{SFR[SED]}}$ which traces the concentration of star formation within the Voronoi bins over a few Myr timescale, and exhibits a large dynamic range among our sample galaxies. A physical example of how patchiness can be used is presented in Fetherolf et al. 2022, where higher patchiness values of stellar reddening indicate a more complex dust distribution.

A burst of star formation on top of an underlying constant SFH can result in an increase in Σ_{SFR}. An element of a resolved population containing a burst of star formation has a higher Σ_{SFR} and a younger stellar age compared to other elements, resulting in a larger $P(\Sigma_{\mathrm{SFR[SED]}})$, and $P(\mathrm{Age})$. Therefore, large $P(\Sigma_{\mathrm{SFR[SED]}})$ may suggest the presence of bursts in localized (Voronoi) regions of galaxies.

3.3 Patchiness of $\Sigma_{\mathrm{SFR[SED]}}$ vs. $L(\mathrm{H}\alpha)/L(\mathrm{UV})$

This section presents our results on the correlation between $P(\Sigma_{\mathrm{SFR[SED]}})$ and $L(\mathrm{H}\alpha)/L(\mathrm{UV})$. Given that star-formation mode varies in strength, duration, or a combination of both factors in different regions of a galaxy (Reddy et al. 2012; Dale et al. 2016, 2020; Smith et al. 2021), and patchiness is sensitive to outliers below and above the average, we expect $P(\Sigma_{\mathrm{SFR[SED]}})$ to be large for galaxies that are undergoing a burst of star formation that could be detected on resolved scales.

Due to surface brightness dimming, higher-redshift objects on average have fewer and larger Voronoi bins. To control for this effect, we divide the MOSDEF sample into two subsmaples in the redshift ranges of $1.37 < z < 1.70$ ($z \sim 1.5$) and $2.09 < z < 2.61$ ($z \sim 2.3$). Figure 3 shows the relationship between $P(\Sigma_{\mathrm{SFR[SED]}})$ and $L(\mathrm{H}\alpha)/L(\mathrm{UV})$ for galaxies in each redshift bin. Based on a Spearman correlation test, we find no significant correlation between the two for both the $z \sim 1.5$ and $z \sim 2.3$ subsamples, with probabilities of $P_{\mathrm{n}} = 0.30$ and 0.36, respectively, of a null correlation. As shown by the stellar age color-coded points, a higher $P(\Sigma_{\mathrm{SFR[SED]}})$ corresponds to a higher $P(\mathrm{Age})$, which is expected given that stellar age and star-formation-rate surface density are correlated for a given SPS model. There is also a lack of correlation between $L(\mathrm{H}\alpha)/L(\mathrm{UV})$ and $P(\mathrm{Age})$ with correlation properties reported in Table 1.

One possible cause for the absence of correlation is the large uncertainties in $L(\mathrm{H}\alpha)/L(\mathrm{UV})$ and $P(\Sigma_{\mathrm{SFR[SED]}})$. Using $L(\mathrm{H}\alpha)/L(\mathrm{UV})$ as a tracer of stochastic star formation may be complicated by uncertainties in dust corrections and aperture mismatches between the Ha and UV measurements (e.g., Brinchmann et al. 2004; Kewley et al. 2005; Salim et al. 2007; Richards et al. 2016; Green et al. 2017; Fetherolf et al. 2022). These issues are discussed in more detail below.

Although there is a consensus that the Cardelli et al. (1989) curve is an adequate description for the dust reddening of nebular recombination lines such as Hα (Reddy et al. 2020; Rezaee et al. 2021), a variety of different stellar attenuation curves have been found for high redshift galaxies, depending on their physical properties. For example, several studies have found that more massive galaxies ($M_* > 10^{10.4}\,M_\odot$) tend to have a slope of the attenuation curve that is similar to the Calzetti et al. (2000), while the SMC extinc-

tion curve has been shown to be applicable for less massive galaxies (Reddy et al. 2015; Du et al. 2018; Shivaei et al. 2020). We obtain the same lack of correlation between $P(\Sigma_{\rm SFR[SED]})$ and $L(\mathrm{H}\alpha)/L(\mathrm{UV})$ when the Reddy et al. (2015) and the metallicity-dependent Shivaei et al. (2020) curves are used to dust-correct $L(\mathrm{UV})$. We find that the degree by which the variation in the attenuation curves affects the $P(\Sigma_{\rm SFR[SED]})$ and $L(\mathrm{H}\alpha)/L(\mathrm{UV})$ correlation is insignificant as long as a fixed curve is assumed to dust-correct $L(\mathrm{UV})$. However, a correlation may still be washed out if the attenuation varies from galaxy to galaxy systematically as a function of $L(\mathrm{H}\alpha)/L(\mathrm{UV})$ ratio.

Another factor that might cause the Hα-to-UV luminosity ratios of high redshift galaxies to deviate from their true values is aperture mismatch. $L(\mathrm{UV})$ is measured using broadband photometry, while Hα luminosity is measured using slit spectroscopy. However, Fetherolf et al. (2021) conducted an aperture-matched analysis utilizing a MOSDEF sample comparable to the one used in this study and found that the variations between Hα and UV SFRs are not caused by the aperture mismatches. Another possible reason for the absence of correlation is that the variations in SFH may be occurring in regions that are still spatially unresolved with the HST imaging (i.e., on scales smaller than a few kpc). Additionally, the lack of correlation could be expected if variations in the SFH are occurring on even shorter timescales than the typical dynamical timescale of the spatial region probed by a Voronoi bin (~ 50 Myr). In this case, such short and localized bursts of star formation may only affect the Hα-to-UV ratio on similar spatial scales.

4 REST-FUV COMPOSITE SPECTRA CONSTRUCTION, AND MODEL-PREDICTED $L(\mathrm{H}\alpha)/L(\mathrm{UV})$

Aside from patchiness, there are several key FUV spectral features that are age-sensitive and can potentially be used to probe bursty SFHs. In this section, we outline a stacking analysis methodology that allows us to measure the average strength of FUV features in bins of $L(\mathrm{H}\alpha)/L(\mathrm{UV})$.

4.1 Rest-FUV Composite Spectra Construction

Rest-FUV spectra are averaged together to produce high S/N composite spectra. Individual LRIS spectra have limited S/N to make measurements on the FUV spectral features. Using the stacked spectra, we measure the average physical properties of galaxies contributing to each composite, as well as measuring FUV spectral features associated with massive stellar populations. We use the procedures that are outlined in Reddy et al. (2016, 2022) to construct the composites. In brief, the science and error spectrum of sample galaxies are shifted to the rest-frame based on the MOSDEF spectroscopic redshift (Section 2.1), converted to luminosity density, and interpolated to a grid with wavelength steps $\Delta\lambda = 0.5$ Å. The composite spectrum at each wavelength point is calculated as the average luminosity density after rejecting 3σ outliers. The error in the composite spectrum is calculated by perturbing the individual spectra according to their error, and using bootstrap resampling to construct the stacked spectrum for those perturbed spectra 100 times. The standard deviation of the luminosity densities at each wavelength point gives the error in the composite spectrum.

4.2 Continuum Normalization

Rest-FUV composite spectra must be continuum-normalized in order to accurately measure the average strength of the FUV stellar features. We use the SPS+Neb models discussed in Reddy et al. (2022) to aid in the normalization process. SPS+Neb models consist of the BPASS SPS models described in Section 2.3 as the stellar component. Each BPASS SPS model is used as an input to the Cloudy[3] version 17.02 radiative transfer code (Ferland et al. 2017) to compute the nebular continuum. The final SPS+Neb models are then built by combining the stellar and nebular components. We refer the reader to Reddy et al. (2022) for more details. In brief, all the BPASS SPS models with a range of stellar ages of $\log[\mathrm{Age/yr}] = \{7.0, 7.3, 7.5, 7.6, 7.8, 8.0, 8.5, 9.0\}$ are interpolated to construct models with stellar metallicities comparable to the values expected for $z \sim 2$ galaxies (Steidel et al. 2016) rather than the original metallicity values of BPASS models described in Section 2.3. This results in a grid of models with stellar metallicities ranging from $Z_* = 10^{-4}$ to 3×10^{-3} spaced by 2×10^{-4}. Our assumptions for the ionization parameter (U) and gas-phase oxygen abundance (i.e., nebular metallicity; $Z_{\rm neb}$) match the average values for the MOSDEF/LRIS sample where $\log[Z_{\rm neb}/Z_\odot] = -0.4$ and $\log U = -3.0$ (Topping et al. 2020; Reddy et al. 2022).

We fit the composite spectra with SPS+Neb models to model the continuum. The SPS+Neb models are normalized for a constant SFR of $1\,M_\odot$/yr. To re-normalize the models to the observed spectra, these models are forced to have the same median luminosity as the composites in the Steidel et al. (2016) "Mask 1" wavelength windows. These wavelength windows are chosen to include regions of the spectrum that are not affected by interstellar absorption and emission features. We smooth the SPS+Neb models for wavelengths below 1500Å to have the same rest-frame resolution as the MOSDEF/LRIS spectra. To identify the best-fit SPS+Neb model for a composite spectrum, the χ^2 between the models and the composite are computed. The model that yields the smallest χ^2 is taken as the best-fit model. Using the median luminosity densities defined in the Rix et al. (2004) wavelength windows, a spline function is fitted to the best-fit model. Finally, the composite spectrum is divided by that spline function to produce a continuum-normalized spectrum.

Any line measurements derived from the continuum-normalized spectra are affected by uncertainties in the normalization of the composite spectra. In order to compute this uncertainty, the normalization process outlined above is applied to 100 realizations of the composite spectrum constructed by bootstrap resampling, and fitting the SPS+Neb models to those realizations. The standard deviation of the best-fit models gives the uncertainty in the continuum normalization at each wavelength point. In addition, all of the model parameters and their uncertainties, including stellar age, metallicity, continuum reddening, and SFR[SED] are derived using the mean and standard deviation of the best-fit values when fitting those realizations, respectively. Figure 4 shows an example of the comparison between the composite spectrum computed for all the galaxies in the MOSDEF/LRIS sample along with SPS+Neb models of different stellar metallicities. Models with lower metallicities are more consistent with the observed composite spectrum of $z \sim 2$ galaxies (Steidel et al. 2016; Reddy et al. 2022).

4.3 $L(\mathrm{H}\alpha)/L(\mathrm{UV})$ Predicted by the SPS+Neb Models versus Physical Properties and Model Assumptions

In this section, we examine how the Hα-to-UV ratio varies with stellar population properties, including stellar age, metallicity, inclusion of binaries, and $M_{\rm cutoff}$ of the IMF using the SPS+Neb models. These relations are shown in Figure 5 and are used to study the systematic

[3] https://gitlab.nublado.org/cloudy/cloudy/-/wikis/home

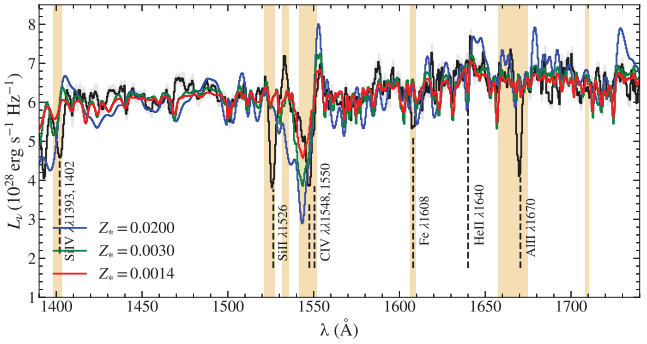

Figure 4. Composite spectrum constructed for the 124 galaxies in the MOSDEF/LRIS sample (black) with 1σ uncertainty (gray). The SPS+Neb models with fixed stellar age of $\log[\mathrm{Age/yr}] = 8.0$ and various stellar metallicities are shown alongside. Some of the prominent FUV spectral features are labeled. Regions that are not included in the fitting process are shaded in orange.

variation observed in $L(\mathrm{H}\alpha)/L(\mathrm{UV})$ of the MOSDEF/LRIS galaxies in Section 5. We calculate the Hα luminosity of each model using the relation:

$$L(\mathrm{H}\alpha)\ [\mathrm{erg\,s^{-1}}] = 1.37 \times 10^{-12}\, N(\mathrm{H}^0)\ [\mathrm{s^{-1}}] \quad (3)$$

where $N(H^0)$ is the hydrogen ionizing photon rate. We calculate $N(H^0)$ by integrating the model spectrum below 912Å. $L(\mathrm{UV})$ is calculated using the SPS+Neb model at $\lambda = 1500$ Å.

The left panel of Figure 5 indicates that the ratio predicted by the constant SFH models ($[L(\mathrm{H}\alpha)/L(\mathrm{UV})]_{\mathrm{SPS+Neb}}$) at a fixed stellar metallicity is influenced by both the choice of upper-mass cutoff of the IMF and inclusion of binary stellar evolution. The Hα luminosity increases by the presence of extremely massive stars with masses greater than $100M_\odot$ and inclusion of energetic binary systems. For example, at $\log[\mathrm{Age/yr}] = 8.0$, the $L(\mathrm{H}\alpha)/L(\mathrm{UV})$ ratio grows by a factor of 1.2, and 1.3, respectively, from "100sin" to the "100bin" and "300bin" models. The number of ionizing photons (and thus $L(\mathrm{H}\alpha)$) will decrease as massive O-stars evolve off the main sequence, whereas less massive stars will still contribute significantly to the non-ionizing UV luminosity. As a result, the $L(\mathrm{H}\alpha)/L(\mathrm{UV})$ ratio decreases with increasing age as shown in the left panel of Figure 5.

The right panel of Figure 5 shows the sensitivity of $[L(\mathrm{H}\alpha)/L(\mathrm{UV})]_{\mathrm{SPS+Neb}}$ of "100bin" model assumption to the stellar metallicity at various stellar population ages of the models. At a fixed stellar age, decreasing stellar metallicity increases the Hα-to-UV luminosity ratio. For example, $[L(\mathrm{H}\alpha)/L(\mathrm{UV})]_{\mathrm{SPS+Neb}}$ grows by a factor of ~ 1.1 from $Z_* = 0.0020$ to $Z_* = 0.0010$ models, at $\log[\mathrm{Age/yr}] = 8.0$. This relationship is expected given that lower-metallicity stellar atmospheres (less opaque) result in higher effective temperatures and therefore harder ionizing spectra (Bicker & Fritze-v. Alvensleben 2005).

5 VARIATIONS OF THE AVERAGE PHYSICAL PROPERTIES OF GALAXIES WITH $L(\mathrm{H}\alpha)/L(\mathrm{UV})$

In addition to variations in the physical properties of galaxies such as stellar age and metallicity, variations in the strength of age-sensitive FUV spectral features with $L(\mathrm{H}\alpha)/L(\mathrm{UV})$ may contain important information on burstiness. To investigate the above-mentioned variations, we divide the MOSDEF/LRIS sample into two $L(\mathrm{H}\alpha)/L(\mathrm{UV})$ subsamples (hereafter referring to as *low*− and *high*−$L(\mathrm{H}\alpha)/L(\mathrm{UV})$ bin) with an equal number of galaxies in each. When binning the galaxies, we are using the Hα-to-UV luminosity ratio rather than the SFR[Hα]-to-SFR[UV] ratio because the latter requires some assumptions of the SFH to convert luminosity to SFR, and when trying to probe the SFH (i.e., whether a galaxy has a bursty or constant SFH), it is useful to use a probe which is independent of such assumptions. The results of the measurements on the two subsamples are presented in the following sections.

5.1 Physical Properties of Galaxies vs. $L(\mathrm{H}\alpha)/L(\mathrm{UV})$

The bestfit SPS+Neb models to the rest-FUV composites are used to derive the average stellar age, metallicity, and continuum reddening of galaxies in each of the $L(\mathrm{H}\alpha)/L(\mathrm{UV})$ bins (Table 2). In order for the SPS+Neb models to self-consistently explain all the observations, we checked that the $L(\mathrm{H}\alpha)/L(\mathrm{UV})$ predicted by the best-fit SPS+Neb model to each composite is in agreement with the mean ratio of all individual galaxies contributing to the composite as well as the average ratio directly measured from the rest-FUV and optical composite spectra [4].

Table 2 reports the average physical properties of galaxies in each $L(\mathrm{H}\alpha)/L(\mathrm{UV})$ bin. Differences in the stellar age and metallicity of the two bins are not significant within the measurement uncertainties showing that the variation observed in the $L(\mathrm{H}\alpha)/L(\mathrm{UV})$ of sample galaxies is unlikely to be tied to the variations in the stellar age or metallicity.

The effective radius (R_e) of each galaxy is taken from van der Wel et al. (2014), and is defined as the radius that contains half of the total $HST/F160W$ light. The star-formation-rate surface density ($\Sigma_{\mathrm{SFR[H}\alpha]}$) of individual galaxies is then computed as:

$$\Sigma_{\mathrm{SFR[H}\alpha]} = \frac{\mathrm{SFR[H}\alpha]}{2\pi R_e^2}. \quad (4)$$

For an ensemble of galaxies, $\langle \mathrm{SFR[H}\alpha] \rangle$ is computed by multiplying the dust-corrected $\langle L(\mathrm{H}\alpha) \rangle$ measured from the optical composite spectrum by the conversion factor determined from the best-fit SPS+Neb model. $\langle \Sigma_{\mathrm{SFR[H}\alpha]} \rangle$ is then computed using $\langle \mathrm{SFR[H}\alpha] \rangle$ and mean R_e of individual galaxies in each ensemble. $\langle \mathrm{SFR[H}\alpha] \rangle$ and $\langle \Sigma_{\mathrm{SFR[H}\alpha]} \rangle$ increase significantly with increasing $\langle L(\mathrm{H}\alpha)/L(\mathrm{UV}) \rangle$ between the two subsamples. While the instantaneous SFR (i.e., SFR[Hα]) differs significantly between the two subsamples, SFR[SED] that covers a timescale of ~ 50 Myr does not change significantly within the measurement uncertainties. This may indicate that the *high*-$L(\mathrm{H}\alpha)/L(\mathrm{UV})$ bin contains objects with higher $L(\mathrm{H}\alpha)$ compared to the *low*-$L(\mathrm{H}\alpha)/L(\mathrm{UV})$ bin, rather than low $L(\mathrm{UV})$. As a consequence, the increase in $\langle \mathrm{SFR[H}\alpha] \rangle$ and $\langle \Sigma_{\mathrm{SFR[H}\alpha]} \rangle$ may be because of the selection criteria of the two subsamples. The difference between the nebular and stellar reddening in the *high*-$L(\mathrm{H}\alpha)/L(\mathrm{UV})$ bin is $\simeq 2.1$ times larger when compared to the *low*-$L(\mathrm{H}\alpha)/L(\mathrm{UV})$. The higher nebular reddening measured for the *high*-$L(\mathrm{H}\alpha)/L(\mathrm{UV})$ bin is not surprising given that galaxies with larger $L(\mathrm{H}\alpha)$ (i.e., higher SFRs) tend to be dustier (Förster Schreiber et al. 2009; Reddy et al. 2010; Kashino et al. 2013; Reddy et al. 2015, 2020).

[4] The same procedure outlined in Section 4.1 is applied to construct the optical composite spectrum (e.g., Shivaei et al. 2018; Reddy et al. 2020; Rezaee et al. 2021). The Python code presented in https://github.com/IreneShivaei/specline/ is used in constructing the optical composite spectra here.

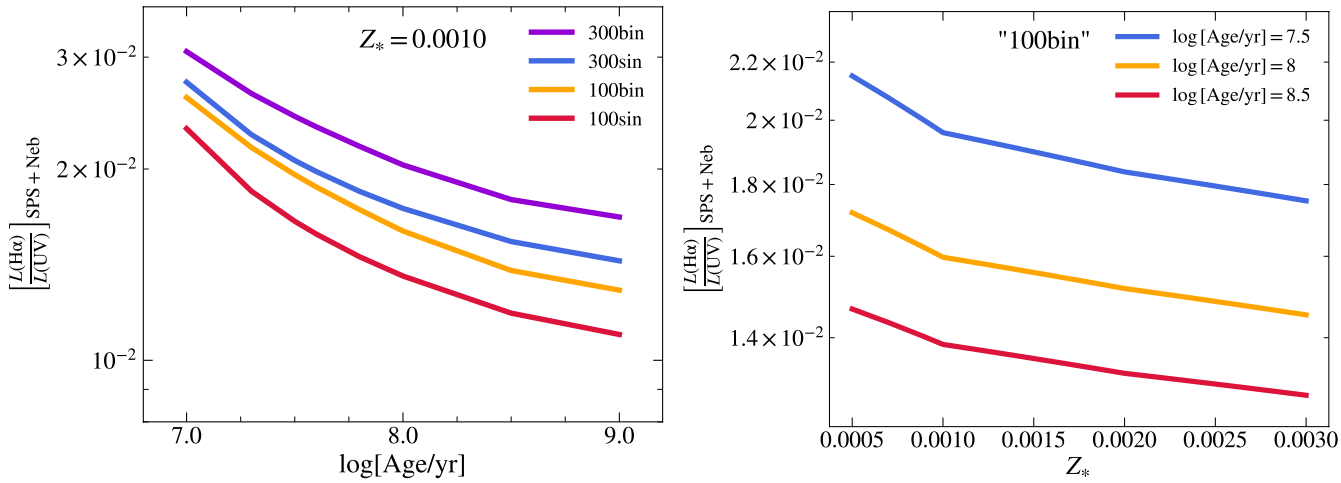

Figure 5. Variation of the Hα-to-UV luminosity ratio derived from the SPS+Neb models with physical properties including stellar age, stellar metallicity, inclusion of binary stellar evolution, and upper-mass cutoff of the IMF.

5.2 Photospheric and stellar wind FUV spectral features vs. $L(\mathrm{H}\alpha)/L(\mathrm{UV})$

Some FUV spectral features are strongly correlated with starburst age, metallicity, and IMF properties, making them excellent proxies for constraining the physical properties of the massive star population (Lamers et al. 1999; Pettini et al. 2000; Leitherer et al. 2001; Mehlert et al. 2002; Smith et al. 2002; Shapley et al. 2003; Keel et al. 2004; Rix et al. 2004; Steidel et al. 2004; Leitherer et al. 2010; Cassata et al. 2013; Gräfener & Vink 2015; Chisholm et al. 2019; Reddy et al. 2022).

In particular, we focus on the photospheric and stellar wind features from massive stars, as these features are strong after a burst of star formation (Walborn et al. 1985; Pellerin et al. 2002; Leitherer 2005; Vidal-García et al. 2017; Calabrò et al. 2021). The FUV spectral features discussed in this work are the P-Cygni component of Si IV $\lambda\lambda$1393, 1402, C IV $\lambda\lambda$1548, 1550, and the stellar component of He II λ1640. The presence of C IV and Si IV P-Cygni features in a galaxy's spectrum suggests the existence of massive stars with $M_* \geqslant 30 M_\odot$ and short main-sequence lifetime of $\sim 2-5$ Myr, and therefore is an indicative of a very recent burst of star formation (Leitherer & Heckman 1995; Pettini et al. 2000; Leitherer et al. 2001; Shapley et al. 2003; Quider et al. 2009). The origin of the broad He II λ1640 stellar wind emission observed in the spectra of local galaxies is the massive short-lived and extremely hot Wolf-Rayet stars (Schaerer 1996; de Mello et al. 1998; Crowther 2007; Shirazi & Brinchmann 2012; Cassata et al. 2013; Visbal et al. 2015; Crowther et al. 2016; Nanayakkara et al. 2019). The fraction of WR stars declines with decreasing stellar metallicity. Therefore, another mechanism is needed to explain the observation of He II λ1640 at high redshift galaxies where the metallicity is lower compared to local galaxies. One possible explanation for such observation is the abundance of binary systems at high redshifts that can result in an increase in the fraction of WR stars in low metallicity environments (Shapley et al. 2003; Cantiello, M. et al. 2007; de Mink et al. 2013). In fact, according to previous studies, when single evolution stellar population synthesis models are compared to the models including binary evolution in low stellar metallicity, the He II stellar feature is best reproduced by the latter (Shirazi & Brinchmann 2012; Steidel et al. 2016; Gutkin et al. 2016; Stanway et al. 2016; Senchyna et al. 2017; Eldridge et al. 2017; Smith et al. 2018; Chisholm et al. 2019; Saxena et al. 2020; Reddy et al. 2022). Therefore, fitting the observed rest-FUV composite spectra with the SPS models that include binary stellar evolution is necessary in order to study the variations in the strength of stellar He II λ1640 emission.

5.2.1 *SPS+Neb Model Predictions of FUV Spectral Features*

Based on the SPS+Neb models, we show an example of the sensitivity of Si IV, C IV, and He II stellar features to the stellar age, metallicity, and M_{cutoff} of the IMF in Figure 6. The equivalent widths (W_λ) of these features are also shown in the inset panels. These equivalent widths are measured by directly integrating across each line (above the line of unity) in the continuum-normalized models. In each panel, we only adjust one physical parameter at a time and keep the other two unchanged. The fixed values are chosen based on the average parameters derived from the composite spectra of all galaxies in the MOSDEF/LRIS sample.

The top panel of Figure 6 compares three constant SFH models with fixed stellar population age of log[Age/yr] = 8.0, fixed upper-mass cutoff of $M_{\mathrm{cutoff}} = 100\,M_\odot$, and varying metallicities of $Z_* = \{0.0010, 0.0020, 0.0030\}$. As depicted by the inset panels, as the metallicity increases from $Z_* = 0.0010$ to $Z_* = 0.0030$, the equivalent widths of C IV and Si IV P-Cygni emission become ~ 2.3 and ~ 2.5 times larger, respectively. This is due to the fact that these P-Cygni features are extremely sensitive to mass-loss rate, which increases as metallicity increases. In the case of He II, the model with lowest metallicity ($Z_* = 0.0010$) exhibits the largest equivalent width compare to the higher metallicity models. This is due to the fact that stars with lower metallicity at given ages have harder ionizing spectra.

The middle panel of Figure 6 shows three models with fixed metallicity of $Z_* = 0.0014$, fixed mass cutoff of $M_{\mathrm{cutoff}} = 100\,M_\odot$, and varying stellar ages of log[Age/yr] = $\{7.0, 7.5, 8.0\}$. The inset panels demonstrate that the younger stellar population model (log[Age/yr] = 7.0) show a larger equivalent width of Si IV, C IV, and He II by a factor of ~ 2.1, ~ 1.6, and ~ 1.5, respectively, when compared to the model with a higher age (log[Age/yr] = 8.0). This prediction again demonstrates that the photospheric and stellar wind spectral features are strong at the early stages of star-formation.

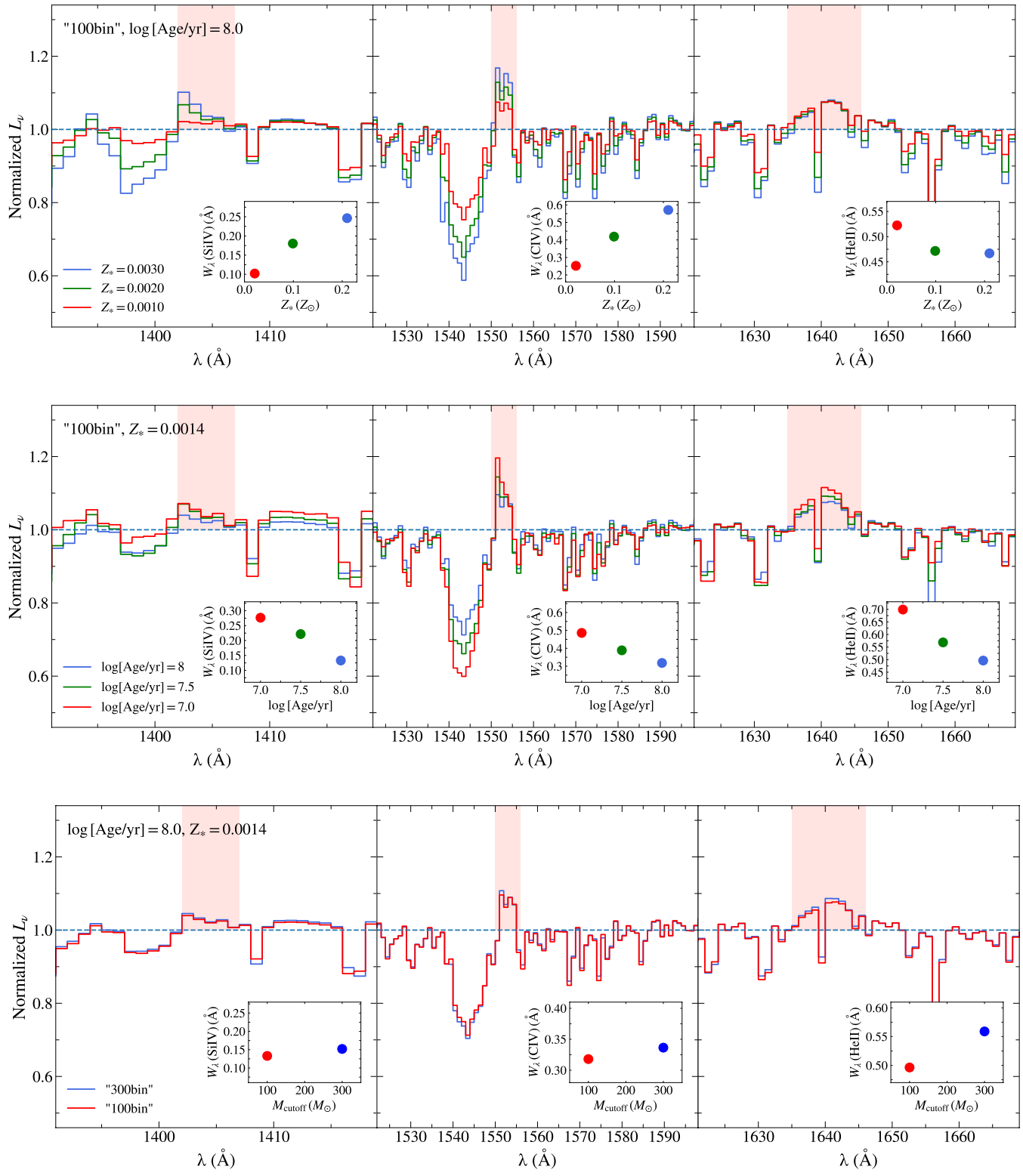

Figure 6. Variation of the continuum-normalized SPS+Neb models with stellar metallicity (*top*), stellar age (*middle*), and upper-mass cutoff of the IMF (*bottom*). In each panel only the specified parameter in the lower left is relaxed to change, while the parameters indicated in the upper left are held fixed. In all panels the ionization parameter and nebular metallicity are held fixed to the average values of the MOSDEF-LRIS sample ($\log U = -3.0$, $\log[Z_{\mathrm{neb}}/Z_\odot] = -0.4$; from Reddy et al. 2022). The inset panels indicate the equivalent width of each line in each model. The shaded pink indicates the regions by which the width measurements are performed for each feature.

Table 2. Average stellar population properties

Properties	*low*-$\frac{L(H\alpha)}{L(UV)}$	*high*-$\frac{L(H\alpha)}{L(UV)}$
$\langle L(\mathrm{H}\alpha)/L(\mathrm{UV})\rangle^{a}$	0.007 ± 0.002	0.035 ± 0.005
$\langle z\rangle^{b}$	2.132 ± 0.031	2.185 ± 0.029
$\langle \log[M_*/M_\odot]\rangle^{c}$	9.88 ± 0.05	9.96 ± 0.06
$\langle R_e\rangle$ (kpc)^{d}	2.94 ± 0.23	2.33 ± 0.14
$\langle 12+\log(\mathrm{O/H})\rangle^{e}$	8.52 ± 0.02	8.39 ± 0.02
$\langle Z_*/Z_\odot\rangle^{f}$	0.099 ± 0.010	0.085 ± 0.015
$\langle \log[\mathrm{Age/yr}]\rangle^{g}$	8.4 ± 0.1	8.0 ± 0.2
$\langle E(B-V)_{\mathrm{cont}}\rangle^{h}$	0.090 ± 0.010	0.074 ± 0.008
$\langle \mathrm{SFR[SED]}\rangle$ ($\mathrm{M_\odot\ yr^{-1}}$)^{i}	9.61 ± 2.73	10.64 ± 3.35
$\langle \mathrm{SFR[H}\alpha\mathrm{]}\rangle$ ($\mathrm{M_\odot\ yr^{-1}}$)^{j}	8.57 ± 1.96	22.12 ± 2.04
$\langle \Sigma_{\mathrm{SFR[H}\alpha\mathrm{]}}\rangle$ ($\mathrm{M_\odot\ yr^{-1}kpc^{-2}}$)^{k}	0.16 ± 0.04	0.65 ± 0.10
$\langle E(B-V)_{\mathrm{neb}}\rangle^{l}$	0.29 ± 0.03	0.49 ± 0.06
$\langle W_\lambda(\mathrm{Si\,IV})\rangle$ (Å)^{m}	0.103 ± 0.018	0.146 ± 0.015
$\langle W_\lambda(\mathrm{C\,IV})\rangle$ (Å)^{n}	0.206 ± 0.034	0.113 ± 0.024
$\langle W_\lambda(\mathrm{He\,II})\rangle$ (Å)^{o}	0.428 ± 0.032	0.684 ± 0.033

[a] Mean dust-corrected Hα-to-UV luminosity ratio.
[b] Mean redshift.
[c] Mean stellar mass.
[d] Mean effective radius.
[e] Mean gas-phase abundances
[f] Stellar metallicity ($Z_\odot$ = 0.0142 from Asplund et al. 2009).
[g] Stellar population age.
[h] Stellar continuum reddening.
[i] SED star-formation rate measured from the FUV composite spectrum.
[j] Hα star-formation rate measured from the optical composite spectrum.
[k] Hα star-formation-rate surface density.
[l] Nebular reddening measured from the optical composite spectrum.
[m] Equivalent width of Si IV $\lambda\lambda$1393, 1403.
[n] Equivalent width of C IV $\lambda\lambda$1548, 1550.
[0] Equivalent width of He II λ1640.

The bottom panel of Figure 6 depicts two SPS+Neb models with fixed stellar age of log[Age/yr] = 8.0 and stellar metallicity of Z_* = 0.0014 and varying upper-mass cutoff of $M_{\mathrm{cutoff}}/M_\odot = \{100, 300\}$. The inset panels indicate that changing the mass cutoff of the IMF from 100 $M_\odot$ to 300 $M_\odot$ causes the equivalent widths of Si IV, C IV, and He II to grow ∼ 1.1, ∼ 1.1, and ∼ 1.2 times larger.

5.2.2 *Observed FUV spectral features in bins of $L(H\alpha)/L(\mathrm{UV})$*

As shown in Section 5.2.1, the model-predicted equivalent widths of Si IV, C IV, and He II are sensitive to stellar age, metallicity, and less sensitive to the high-mass cutoff of the IMF. In this section, we examine the variations in the observed equivalent widths of those FUV spectral features from the composite spectra of the two $L(\mathrm{H}\alpha)/L(\mathrm{UV})$ subsamples. The advantage of analyzing equivalent widths of the observed features is that they are unaffected by dust or aperture uncertainties. In addition, the observed equivalent widths are insensitive to the model assumptions (e.g., constant vs. instantaneous burst SFH).

The average rest-frame equivalent widths ($\langle W_\lambda\rangle$) for each of the above-mentioned FUV spectral features are measured by directly integrating across each line in each of the continuum-normalized composite spectra shown in Figure 7 and are reported in Table 2. To ensure unbiased measurements, we utilize identical wavelength intervals for each bin. These wavelength intervals are derived based on the regions that the lines occupy in the SPS+Neb models. These regions are highlighted in Figure 6. The errors in W_λ are measured by perturbing the continuum-normalized spectra according to the error in spectra and repeating the measurements many times. The uncertainty is determined by the standard deviation of these perturbations. The final reported uncertainties include the error associated with the normalization process.

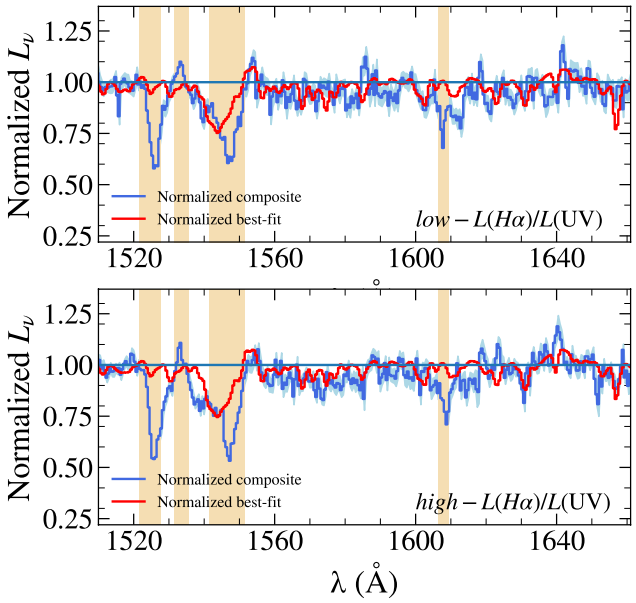

Figure 7. Continuum-normalized composite spectra (*blue*) of the two $L(\mathrm{H}\alpha)/L(\mathrm{UV})$ subsamples from which the equivalent width measurements are performed. The physical properties of each of the bins, as well as, W_λ(Si IV), W_λ(C IV), and W_λ(He II) measurements are listed in Table 2. Those regions that are not included in the fitting process are shaded in orange.

Figure 8 shows the comparison between the average rest-frame equivalent widths of Si IV, C IV, and He II in the $L(\mathrm{H}\alpha)/L(\mathrm{UV})$ subsamples. No significant differences are found in $\langle W_\lambda(\mathrm{Si\,IV})\rangle$, and $\langle W_\lambda(\mathrm{C\,IV})\rangle$ between the *low*- and *high*-$L(\mathrm{H}\alpha)/L(\mathrm{UV})$ bins within the measurement uncertainties. However, $\langle W_\lambda(\mathrm{He\,II})\rangle$ grows by a factor of ∼ 1.7 from the *low*- to *high*-$L(\mathrm{H}\alpha)/L(\mathrm{UV})$ bin. If galaxies with higher $L(\mathrm{H}\alpha)/L(\mathrm{UV})$ are undergoing a burst of star formation, then we would expect them to have higher C IV and Si IV P-Cygni emission equivalent widths relative to galaxies with lower $L(\mathrm{H}\alpha)/L(\mathrm{UV})$.

While Si IV and C IV P-Cygni emissions are prominently stellar in origin, this is not the case for He II. The extremely hot sources that produce stellar He II emission also generate enough $\mathrm{He^+}$ ionizing photons with wavelengths of $\lambda < 228$ Å to yield nebular He II emission due to recombination, which complicates the interpretation of the He II emission. Based on the previous studies (e.g., Steidel et al. 2016; Reddy et al. 2022), we adopt the following procedure to disentangle the stellar and nebular components. We measure the observed nebular He II intensity by subtracting the best-fit SPS+Neb model from the composite spectrum of each bin using the "100bin" and "300bin" [5] model assumptions. Because the best-fit

[5] When fitting the FUV composite spectra with the "300bin" SPS+Neb models, they can still reproduce all the FUV features discussed in this work.

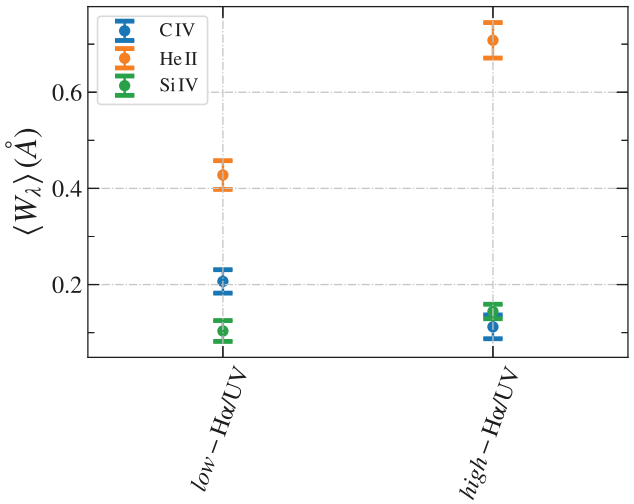

Figure 8. Comparison of the average equivalent widths of Si IV $\lambda\lambda$1393, 1402 , C IV $\lambda\lambda$1548, 1550, and He II λ1640 stellar emission lines measured from the continuum-normalized spectra of the two bins reported in Table 2.

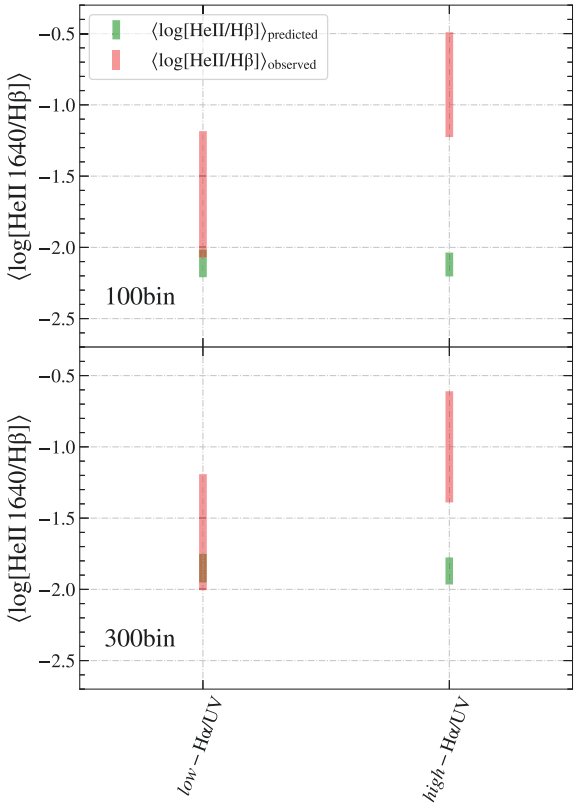

Figure 9. Comparison of the model-predicted nebular He II λ1640 relative intensity, $\langle$He II/H$\beta\rangle$, derived from the Cloudy code and the observed dust-corrected relative intensity measured by subtraction of the best-fit SPS+Neb model from the composite spectrum for each $L(\mathrm{H}\alpha)/L(\mathrm{UV})$ subsample and different model assumptions. The colored bars show the $\pm 3\sigma$ range of the measurement uncertainties.

model identifies the stellar component, the subtraction of the best-fit model from the observed spectrum is assumed to be purely nebular. The observed nebular He II intensity is then dust-corrected assuming $\langle E(B-V)_{\mathrm{neb}}\rangle$ and the Cardelli et al. (1989) extinction curve, where $\langle E(B-V)_{\mathrm{neb}}\rangle$ is measured directly from the optical composite spectrum. The model-predicted nebular He II intensity is derived by using the best-fit SPS model of each bin as an input to the Cloudy photoionization code. The comparison between the model-predicted and observed nebular He II emission in terms of relative intensity, $\langle$He II/H$\beta\rangle$, is shown in Figure 9 for the $L(\mathrm{H}\alpha)/L(\mathrm{UV})$ subsamples. The model-predicted and observed nebular He II intensities measured for the *low*-$L(\mathrm{H}\alpha)/L(\mathrm{UV})$ bin agree within the 3σ uncertainty for both of the mass cutoff assumptions. However, the model prediction of the nebular He II intensity does not fully account for the observed nebular He II intensity in the *high*-$L(\mathrm{H}\alpha)/L(\mathrm{UV})$ bin even with an increase in the upper-mass cutoff of the IMF.

Our results indicate that recent SF activity, and low metallicity cannot explain the difference in the He II emission of galaxies in the two $L(\mathrm{H}\alpha)/L(\mathrm{UV})$ bins because the stellar age and metallicity derived for the two bins are similar within their respective uncertainties. Next, we investigate whether a top heavy IMF can account for such a difference. First, we separate the nebular and stellar components of the He II emission. We then compare the observed nebular He II intensity to that predicted by the Cloudy photoionization model using various assumptions on the upper-mass limit of the IMF. We find that even a top heavy IMF model ($M_{\mathrm{cutoff}} = 300 M_\odot$) is unable to accurately predict the observed nebular He II intensity of the *high*-$L(\mathrm{H}\alpha)/L(\mathrm{UV})$ bin. Another potential contributor that gives rise to the He^+ ionizing photons budget in low-metallicity star-forming galaxies is discussed below.

Schaerer et al. (2019) suggested that high mass X-ray binaries (HMXBs) are a primary source for producing He^+ ionizing photons in low-metallicity star-forming galaxies. They found that only SPS models that include HMXBs are able to reproduce the observed relative intensity of nebular He II emission (He II/Hβ). Studies of both the local and high-redshift universe have suggested that the X-ray luminosity (L_{X}) of HMXBs in star-forming galaxies increases with SFR (Nandra et al. 2002; Bauer et al. 2002; Seibert et al. 2002; Grimm et al. 2003; Reddy & Steidel 2004; Persic et al. 2004; Gilfanov et al. 2004; Persic & Rephaeli 2007; Lehmer et al. 2008, 2010), which is expected owing to the young ages of HXMBs ($\sim$ 10 Myr). Several studies have indicated that L_{X} per unit SFR in star-forming galaxies elevates at high redshift (e.g., Basu-Zych et al. 2013a; Lehmer et al. 2016; Aird et al. 2017). This enhancement in L_{X}/SFR with redshift may be due to the lower metallicities of high-redshift galaxies, which results in more luminous (and possibly more numerous) HMXBs (Brorby et al. 2016; Douna et al. 2015). In fact, observational studies have shown evidence of several ultraluminous X-ray sources in nearby galaxies with low metallicities (e.g., Mineo et al. 2012; Prestwich et al. 2013; Basu-Zych et al. 2013b). Following the idea that L_{X}/SFR is metallicity-dependent, Brorby et al. (2016) parameterized the L_{X}-SFR-Z relationship, where Z is the gas-phase metallicity, for a sample of local star-forming galaxies as:

The best-fit stellar population age, metallicity, and continuum reddening of the *high*-$L(\mathrm{H}\alpha)/L(\mathrm{UV})$ subsample obtained with the "300bin" model are $\langle \log[\mathrm{Age/yr}]\rangle = 8.0 \pm 0.2$, $\langle Z_*\rangle = 0.084 \pm 0.011$, and $\langle E(B-V)_{\mathrm{cont}}\rangle = 0.067 \pm 0.005$.

$$\log\left(\frac{L_X/\mathrm{SFR}}{\mathrm{erg\,s^{-1}}/(\mathrm{M_\odot\,yr^{-1}})}\right) = -0.59\times(12+\log(\mathrm{O/H})-8.69) +39.49. \quad (5)$$

Fornasini et al. (2019) studied a sample of MOSDEF galaxies with available X-ray data to investigate the L_X/SFR and Z relationship at redshift $z\sim2$. They found that L_X/SFR—for SFRs that are computed using the Hα line—are consistent with the Brorby et al. (2016) L_X-SFR-Z relation (Equation 5). Hence, we use Equation 5 to calculate the average X-ray luminosities of the $L(\mathrm{H}\alpha)/L(\mathrm{UV})$ subsamples. The mean X-ray luminosity of the *low-* and *high-*$L(\mathrm{H}\alpha)/L(\mathrm{UV})$ bins are $\langle L_X\rangle = (3.3\pm0.6)$, and $(10.3\pm1.1)\times10^{40}$ erg s^{-1}, respectively. The increase in $\langle L_X\rangle$ with increasing $L(\mathrm{H}\alpha)/L(\mathrm{UV})$ may indicate the presence of luminous HMXBs, which in turn could explain the high nebular He II emission observed for galaxies with high $L(\mathrm{H}\alpha)/L(\mathrm{UV})$ ratios.

6 SUMMARY AND CONCLUSION

We examine the effectiveness of the dust-corrected globally measured Hα-to-UV luminosity ratio in tracing burstiness for typical star-forming galaxies at $z\sim2$. We use the MOSDEF survey to explore stellar population properties differences in bins of $L(\mathrm{H}\alpha)/L(\mathrm{UV})$.

In the first part of this analysis, we employ the HST imaging of 310 star-forming galaxies (MOSDEF/MORPH sample) drawn from the MOSDEF survey to construct the star-formation-rate surface density and stellar age maps. We use a Voronoi binning technique to group the pixels based on their S/N. We then study the distribution of $\Sigma_{\mathrm{SFR[SED]}}$ and stellar age of Voronoi bins within each galaxy using a morphological metric called patchiness (P). Patchiness is sensitive to deviations from average, therefore galaxies that are undergoing a burst of star-formation contain regions with higher $\Sigma_{\mathrm{SFR[SED]}}$ and younger stellar age than the mean value for the entire galaxy and are expected to exhibit higher $P(\Sigma_{\mathrm{SFR[SED]}})$ and/or $P(\mathrm{Age})$. We find no correlation between $L(\mathrm{H}\alpha)/L(\mathrm{UV})$ and $P(\Sigma_{\mathrm{SFR[SED]}})$, as well as between $L(\mathrm{H}\alpha)/L(\mathrm{UV})$ and $P(\mathrm{Age})$. We suggest that $L(\mathrm{H}\alpha)/L(\mathrm{UV})$ does not trace stochastic SFH over a time-scale of ~50 Myr which is the timescale probed by the Voronoi bins. We suggest that this lack of correlation may be because of the uncertainties related to the variations in the stellar dust attenuation curve, limited dynamical time scale and spatial resolution probed by the Voronoi bins.

In the second part of this analysis, we use a rest-FUV spectroscopic sample obtained by LRIS (MOSDEF/LRIS sample) to study the average physical properties of $z\sim2$ star-forming galaxies in bins of $L(\mathrm{H}\alpha)/L(\mathrm{UV})$. We use the `BPASS` constant SFH models combined with the nebular continuum emission generated by the `Cloudy` radiative transfer code (`SPS+Neb` models) as our theoretical basis to address the effect of different physical assumptions on the model-predicted $L(\mathrm{H}\alpha)/L(\mathrm{UV})$. As suggested by other studies, the Hα-to-UV ratio predicted by `SPS+Neb` models increases for younger stellar populations, or when the upper end of the IMF increases. Inclusion of binary stellar evolution or lowering the stellar metallicity of the models also cause a rise in the predicted ratio. We divide the 124 galaxies in the MOSDEF/LRIS sample into two bins of $L(\mathrm{H}\alpha)/L(\mathrm{UV})$ with an equal number of galaxies in each to investigate whether the variation observed in the dust-corrected Hα-to-UV ratio is related to differences in stellar age, metallicity, and/or upper end mass of the IMF as suggested by the SPS theoretical models. The main conclusions of the second part of the paper are as follows:

- We find no significant variation in the stellar population age and metallicity between the *low-* and *high-*$L(\mathrm{H}\alpha)/L(\mathrm{UV})$ bin within the measurement uncertainties. Based on this result we cannot attribute the variations observed in the dust-corrected Hα-to-UV ratio of the sample galaxies to the recent burst activities and/or differences in the stellar metallicity (i.e., hardness of the ionizing spectrum).
- The average SFR[Hα] and $\Sigma_{\mathrm{SFR[H}\alpha]}$ increase significantly from the *low-* to *high-*$L(\mathrm{H}\alpha)/L(\mathrm{UV})$ bin, while the average SFR[SED] remains unchanged within the measurement uncertainties. We suggest the selection criteria between the two $L(\mathrm{H}\alpha)/L(\mathrm{UV})$ subsamples is the reason for the observed increases in $\langle\mathrm{SFR[H}\alpha]\rangle$ and $\langle\Sigma_{\mathrm{SFR[H}\alpha]}\rangle$, as the *high-*$L(\mathrm{H}\alpha)/L(\mathrm{UV})$ selects galaxies with high $L(\mathrm{H}\alpha)$.
- We measure the observed equivalent widths of the Si IV $\lambda\lambda$1393, 1402, C IV $\lambda\lambda$1548, 1550, and He II λ1640 emission lines for the two $L(\mathrm{H}\alpha)/L(\mathrm{UV})$ bins as these features are extremely sensitive to stellar population age, and metallicity. We find no significant variations between the EWs of the C IV and Si IV P-Cygni emissions observed in the composite spectra of the two $L(\mathrm{H}\alpha)/L(\mathrm{UV})$ bins. The EW of the He II λ1640 emission grows significantly from the *low-* to *high-*$L(\mathrm{H}\alpha)/L(\mathrm{UV})$ bin. The lack of variations in the strength of the P-Cygni emissions between the two $L(\mathrm{H}\alpha)/L(\mathrm{UV})$ subsamples is expected given the insignificant differences found between the stellar age and metallicity of the two subsamples.
- The difference between the strength of the observed He II emission of the *low-* and *high-*$L(\mathrm{H}\alpha)/L(\mathrm{UV})$ subsamples can be further investigated when the nebular and stellar components of the He II line are disentangled. We find that the model-predicted nebular He II intensity cannot accurately predict the observed amount for the *high-*$L(\mathrm{H}\alpha)/L(\mathrm{UV})$ bin even if the upper-mass limit of the IMF is increased from $M_{\mathrm{cutoff}}=100\,M_\odot$ to $300\,M_\odot$. According to recent studies, low metallicity star-forming galaxies get the majority of their He^+ ionizing photons from high mass X-ray binaries (Schaerer et al. 2019). We measure the X-ray luminosity of each bin using the L_X-SFR-Z relation found by Brorby et al. (2016). We find that the X-ray luminosity is on average larger for galaxies with higher $L(\mathrm{H}\alpha)/L(\mathrm{UV})$. This result may suggest the presence of luminous HMXBs, which could explain the high nebular He II emission observed for galaxies with high Hα-to-UV ratios.

In this work, we find no strong evidence for the dust-corrected Hα-to-UV ratio to be tracing burstiness. There is one important implication of this work. It is proposed that star-forming galaxies may be in a bursty phase of star formation at the beginning of the reionization epoch, producing enough ionizing photons to reionize the intergalactic medium. If such is the case, it is important to validate the tracer of burstiness which commonly used in the literature, and whether there are other phenomenon that can affect the Hα-to-UV ratio. Using the next generation telescopes, we will have access to even more high quality data to study the Hα-to-UV ratio variations in more details. For example, James Webb Space Telescope can provide high resolution rest-FUV spectra of high redshift galaxies to aid constraining the mode of star formation history and/or hardness of the ionizing spectrum and the causes of the variations in the Hα-to-UV ratio.

Several studies of high redshift galaxies have found evidence of bursty SFHs by comparing Hα and UV SFRs (e.g., Atek et al. 2022 at $z\sim1.1$, and Faisst et al. 2019 at $z\sim4.5$). These works suggest that the excess found in the Hα SFR relative to the UV SFR can only be explained by additional bursts of star formation on top of an underlying smooth star formation. The aforementioned studies have found that SFR[Hα]/SFR[UV] ratio is preferentially higher for lower mass galaxies. Galaxies of lower masses, which are also likely to have a lower metallicity, may be conducive to an IMF that is

top-heavy (Tremonti et al. 2004; Dalcanton 2007; Lara-López et al. 2010; Peeples & Shankar 2011; Lilly et al. 2013; Andrews & Martini 2013; Zahid et al. 2014; Chisholm et al. 2018), and therefore one must be very careful in interpreting the Hα-to-UV ratio for such galaxies. The equivalent width of the stellar photosphere features studied in this work (Section 5.2) are less affected by the source of uncertainties listed for the Hα-to-UV ratio including variation of the ionizing escape fraction, stochastic IMF, and dust reddening. Hence, the equivalent width of FUV stellar features (e.g., C IV, and Si IV) may more reliably trace recent bursts of star formation than the Hα-to-UV ratio.

ACKNOWLEDGEMENTS

This work is based on observations taken by the 3D-HST Treasury Program (GO 12177 and 12328) with the NASA/ESA HST, which is operated by the Association of Universities for Research in Astronomy, Inc., under NASA contract NAS5-26555. In addition, we would like to acknowledge that this work made use of v2.2.1 of the Binary Population and Spectral Synthesis (BPASS) models as described in Eldridge et al. (2017), and Stanway & Eldridge (2018). The MOSDEF team acknowledges support from an NSF AAG collaborative grant (AST-1312780, 1312547, 1312764, and 1313171), grant AR-13907 from the Space Telescope Science Institute, grant NNX16AF54G from the NASA ADAP program, and Chandra archival award AR6-17011X. This work would not have been possible without the generous contributions from the 3D-HST collaboration. The MOSDEF data were obtained at the W.M. Keck Observatory, which is operated as a scientific partnership among the California Institute of Technology, the University of California and the National Aeronautics and Space Administration. The Observatory was made possible by the generous financial support of the W.M. Keck Foundation. We recognize and acknowledge the very significant cultural role and reverence that the summit of Mauna Kea has always had within the indigenous Hawaiian community. We are most fortunate to have the opportunity to conduct observations from this mountain.

DATA AVAILABILITY

In this work, we use spectroscopic redshifts and rest-frame optical line measurements obtained from the MOSFIRE Deep Evolution Field (MOSDEF) survey (Kriek et al. 2015). This is publicly available at https://mosdef.astro.berkeley.edu/.

We also use photometry obtained from the CANDELS (Grogin et al. 2011; Koekemoer et al. 2011) and reprocessed by the 3D-HST grism survey team (Brammer et al. 2012; Skelton et al. 2014; Momcheva et al. 2016). The data sets and catalogs can be found at https://archive.stsci.edu/prepds/3d-hst/.

We analyze the Far-UV spectra obtained by the Low Resolution Imagerand Spectrometer (LRIS; Oke et al. 1995; Steidel et al. 2004). Topping et al. (2020) and Reddy et al. (2022) contain information about the MOSDEF/LRIS data reduction. MOSDEF/LRIS data sets are available upon request.

REFERENCES

Aird J., Coil A. L., Georgakakis A., 2017, MNRAS, 465, 3390
Andrews B. H., Martini P., 2013, ApJ, 765, 140
Asplund M., Grevesse N., Sauval A. J., Scott P., 2009, Annual Review of Astronomy and Astrophysics, 47, 481
Asquith R., et al., 2018, MNRAS, 480, 1197
Atek H., Furtak L. J., Oesch P., van Dokkum P., Reddy N., Contini T., Illingworth G., Wilkins S., 2022, MNRAS, 511, 4464
Azadi M., et al., 2017, ApJ, 835, 27
Azadi M., et al., 2018, ApJ, 866, 63
Basu-Zych A. R., et al., 2013a, ApJ, 762, 45
Basu-Zych A. R., et al., 2013b, ApJ, 774, 152
Bauer F. E., Alexander D. M., Brandt W. N., Hornschemeier A. E., Vignali C., Garmire G. P., Schneider D. P., 2002, AJ, 124, 2351
Bertin, E. Arnouts, S. 1996, Astron. Astrophys. Suppl. Ser., 117, 393
Bicker J., Fritze-v. Alvensleben U., 2005, A&A, 443, L19
Boselli A., Boissier S., Cortese L., Buat V., Hughes T. M., Gavazzi G., 2009, ApJ, 706, 1527
Brammer G. B., et al., 2012, ApJS, 200, 13
Brinchmann J., Charlot S., White S. D. M., Tremonti C., Kauffmann G., Heckman T., Brinkmann J., 2004, MNRAS, 351, 1151
Brorby M., Kaaret P., Prestwich A., Mirabel I. F., 2016, MNRAS, 457, 4081
Calabrò A., et al., 2021, A&A, 646, A39
Calzetti D., Armus L., Bohlin R. C., Kinney A. L., Koornneef J., Storchi-Bergmann T., 2000, ApJ, 533, 682
Cantiello, M. Yoon, S.-C. Langer, N. Livio, M. 2007, A&A, 465, L29
Caplar N., Tacchella S., 2019, MNRAS, 487, 3845
Cappellari M., Copin Y., 2003, Monthly Notices of the Royal Astronomical Society, 342, 345
Cardelli J. A., Clayton G. C., Mathis J. S., 1989, ApJ, 345, 245
Cassata P., et al., 2013, A&A, 556, A68
Chabrier G., 2003, PASP, 115, 763
Chisholm J., Tremonti C., Leitherer C., 2018, MNRAS, 481, 1690
Chisholm J., Rigby J. R., Bayliss M., Berg D. A., Dahle H., Gladders M., Sharon K., 2019, The Astrophysical Journal, 882, 182
Choi J., Conroy C., Byler N., 2017, ApJ, 838, 159
Coil A. L., et al., 2015, ApJ, 801, 35
Crowther P. A., 2007, ARA&A, 45, 177
Crowther P. A., et al., 2016, MNRAS, 458, 624
Dalcanton J. J., 2007, The Astrophysical Journal, 658, 941
Dale D. A., et al., 2016, AJ, 151, 4
Dale D. A., et al., 2020, AJ, 159, 195
Dickey C. M., et al., 2021, ApJ, 915, 53
Dobbs C. L., Pringle J. E., 2009, MNRAS, 396, 1579
Domínguez A., Siana B., Brooks A. M., Christensen C. R., Bruzual G., Stark D. P., Alavi A., 2015, MNRAS, 451, 839
Douna V. M., Pellizza L. J., Mirabel I. F., Pedrosa S. E., 2015, A&A, 579, A44
Du X., et al., 2018, ApJ, 860, 75
Eldridge J. J., 2012, MNRAS, 422, 794
Eldridge J. J., Stanway E. R., Xiao L., McClelland L. A. S., Taylor G., Ng M., Greis S. M. L., Bray J. C., 2017, Publ. Astron. Soc. Australia, 34, e058
Elmegreen B. G., 2006, ApJ, 648, 572
Emami N., Siana B., Weisz D. R., Johnson B. D., Ma X., El-Badry K., 2019, The Astrophysical Journal, 881, 71
Faisst A. L., Capak P. L., Emami N., Tacchella S., Larson K. L., 2019, ApJ, 884, 133
Feldmann R., Quataert E., Hopkins P. F., Faucher-Giguère C.-A., Kereš D., 2017, MNRAS, 470, 1050
Ferland G. J., et al., 2017, Rev. Mex. Astron. Astrofis., 53, 385
Fetherolf T., et al., 2020, MNRAS, 498, 5009
Fetherolf T., et al., 2021, MNRAS, 508, 1431
Fitzpatrick E. L., Massa D., 1990, ApJS, 72, 163
Fornasini F. M., et al., 2019, ApJ, 885, 65
Förster Schreiber N. M., et al., 2009, ApJ, 706, 1364
Freeman W. R., et al., 2017, arXiv e-prints, p. arXiv:1710.03230
Fudamoto Y., et al., 2020, A&A, 643, A4
Fujimoto Y., Chevance M., Haydon D. T., Krumholz M. R., Kruijssen J. M. D., 2019, MNRAS, 487, 1717
Fumagalli M., da Silva R. L., Krumholz M. R., 2011, ApJ, 741, L26
Genzel R., et al., 2010, MNRAS, 407, 2091
Gilfanov M., Grimm H. J., Sunyaev R., 2004, MNRAS, 347, L57

Glazebrook K., Blake C., Economou F., Lilly S., Colless M., 1999, MNRAS, 306, 843
Gordon K. D., Clayton G. C., Misselt K. A., Landolt A. U., Wolff M. J., 2003, ApJ, 594, 279
Governato F., et al., 2010, Nature, 463, 203
Gräfener G., Vink J. S., 2015, A&A, 578, L2
Green A. W., Glazebrook K., Gilbank D. G., McGregor P. J., Damjanov I., Abraham R. G., Sharp R., 2017, MNRAS, 470, 639
Grimm H. J., Gilfanov M., Sunyaev R., 2003, MNRAS, 339, 793
Grogin N. A., et al., 2011, ApJS, 197, 35
Gutkin J., Charlot S., Bruzual G., 2016, MNRAS, 462, 1757
Hayward C. C., Hopkins P. F., 2017, MNRAS, 465, 1682
Hemmati S., et al., 2014, The Astrophysical Journal, 797, 108
Hopkins A. M., Beacom J. F., 2006, ApJ, 651, 142
Hopkins P. F., Kereš D., Oñorbe J., Faucher-Giguère C.-A., Quataert E., Murray N., Bullock J. S., 2014, MNRAS, 445, 581
Hoversten E. A., Glazebrook K., 2008, ApJ, 675, 163
Hunter D. A., Elmegreen B. G., Ludka B. C., 2010, AJ, 139, 447
Iglesias-Páramo J., Boselli A., Gavazzi G., Zaccardo A., 2004, A&A, 421, 887
Jafariyazani M., Mobasher B., Hemmati S., Fetherolf T., Khostovan A. A., Chartab N., 2019, ApJ, 887, 204
Kashino D., et al., 2013, ApJ, 777, L8
Keel W. C., Holberg J. B., Treuthardt P. M., 2004, AJ, 128, 211
Kennicutt Robert C. J., 1989, ApJ, 344, 685
Kennicutt R. C., Evans N. J., 2012, ARA&A, 50, 531
Kereš D., Katz N., Davé R., Fardal M., Weinberg D. H., 2009, MNRAS, 396, 2332
Kewley L. J., Geller M. J., Jansen R. A., Dopita M. A., 2002, AJ, 124, 3135
Kewley L. J., Jansen R. A., Geller M. J., 2005, PASP, 117, 227
Knapen J. H., James P. A., 2009, The Astrophysical Journal, 698, 1437
Koekemoer A. M., et al., 2011, The Astrophysical Journal Supplement Series, 197, 36
Kriek M., et al., 2015, The Astrophysical Journal Supplement Series, 218, 15
Lamers H. J. G. L. M., Haser S., de Koter A., Leitherer C., 1999, ApJ, 516, 872
Lara-López M. A., et al., 2010, A&A, 521, L53
Lee J. C., et al., 2009, The Astrophysical Journal, 706, 599
Lee J. C., et al., 2011, ApJS, 192, 6
Lehmer B. D., et al., 2008, ApJ, 681, 1163
Lehmer B. D., Alexander D. M., Bauer F. E., Brandt W. N., Goulding A. D., Jenkins L. P., Ptak A., Roberts T. P., 2010, ApJ, 724, 559
Lehmer B. D., et al., 2016, ApJ, 825, 7
Leitherer C., 2005, A Far-Ultraviolet View of Starburst Galaxies. p. 89, doi:10.1007/1-4020-3539-X_16
Leitherer C., Heckman T. M., 1995, ApJS, 96, 9
Leitherer C., Leão J. R. S., Heckman T. M., Lennon D. J., Pettini M., Robert C., 2001, ApJ, 550, 724
Leitherer C., Ortiz Otálvaro P. A., Bresolin F., Kudritzki R.-P., Lo Faro B., Pauldrach A. W. A., Pettini M., Rix S. A., 2010, ApJS, 189, 309
Leung G. C. K., et al., 2019, ApJ, 886, 11
Lilly S. J., Carollo C. M., Pipino A., Renzini A., Peng Y., 2013, ApJ, 772, 119
Ma X., et al., 2018, MNRAS, 478, 1694
Madau P., Dickinson M., 2014, Annual Review of Astronomy and Astrophysics, 52, 415
Madau P., Ferguson H. C., Dickinson M. E., Giavalisco M., Steidel C. C., Fruchter A., 1996, MNRAS, 283, 1388
Mas-Ribas L., Dijkstra M., Forero-Romero J. E., 2016, The Astrophysical Journal, 833, 65
McLean I. S., et al., 2012, in McLean I. S., Ramsay S. K., Takami H., eds, Society of Photo-Optical Instrumentation Engineers (SPIE) Conference Series Vol. 8446, Ground-based and Airborne Instrumentation for Astronomy IV. p. 84460J, doi:10.1117/12.924794
Mehlert D., et al., 2002, A&A, 393, 809
Meurer G. R., et al., 2009, The Astrophysical Journal, 695, 765
Mineo S., Gilfanov M., Sunyaev R., 2012, MNRAS, 419, 2095
Momcheva I. G., et al., 2016, ApJS, 225, 27
Nanayakkara T., et al., 2019, A&A, 624, A89
Nandra K., Mushotzky R. F., Arnaud K., Steidel C. C., Adelberger K. L., Gardner J. P., Teplitz H. I., Windhorst R. A., 2002, The Astrophysical Journal, 576, 625
Noeske K. G., et al., 2007, ApJ, 660, L43
Oke J. B., et al., 1995, PASP, 107, 375
Papovich C., Dickinson M., Ferguson H. C., 2001, ApJ, 559, 620
Peeples M. S., Shankar F., 2011, MNRAS, 417, 2962
Pellerin A., et al., 2002, ApJS, 143, 159
Persic M., Rephaeli Y., 2007, A&A, 463, 481
Persic M., Rephaeli Y., Braito V., Cappi M., Della Ceca R., Franceschini A., Gruber D. E., 2004, A&A, 419, 849
Pettini M., Steidel C. C., Adelberger K. L., Dickinson M., Giavalisco M., 2000, ApJ, 528, 96
Pflamm-Altenburg J., Weidner C., Kroupa P., 2007, ApJ, 671, 1550
Pflamm-Altenburg J., Weidner C., Kroupa P., 2009, MNRAS, 395, 394
Prestwich A. H., Tsantaki M., Zezas A., Jackson F., Roberts T. P., Foltz R., Linden T., Kalogera V., 2013, ApJ, 769, 92
Quider A. M., Pettini M., Shapley A. E., Steidel C. C., 2009, MNRAS, 398, 1263
Reddy N. A., Steidel C. C., 2004, ApJ, 603, L13
Reddy N. A., Erb D. K., Pettini M., Steidel C. C., Shapley A. E., 2010, ApJ, 712, 1070
Reddy N. A., Pettini M., Steidel C. C., Shapley A. E., Erb D. K., Law D. R., 2012, The Astrophysical Journal, 754, 25
Reddy N. A., et al., 2015, ApJ, 806, 259
Reddy N. A., Steidel C. C., Pettini M., Bogosavljević M., 2016, ApJ, 828, 107
Reddy N. A., et al., 2018, ApJ, 853, 56
Reddy N. A., et al., 2020, ApJ, 902, 123
Reddy N. A., et al., 2022, ApJ, 926, 31
Rezaee S., Reddy N., Shivaei I., Fetherolf T., Emami N., Khostovan A. A., 2021, Monthly Notices of the Royal Astronomical Society, 506, 3588
Richards S. N., et al., 2016, MNRAS, 455, 2826
Rix S. A., Pettini M., Leitherer C., Bresolin F., Kudritzki R.-P., Steidel C. C., 2004, ApJ, 615, 98
Rodighiero G., et al., 2014, MNRAS, 443, 19
Salim S., et al., 2007, ApJS, 173, 267
Saxena A., et al., 2020, A&A, 636, A47
Schaerer D., 1996, ApJ, 467, L17
Schaerer D., Fragos T., Izotov Y. I., 2019, A&A, 622, L10
Schmidt M., 1959, ApJ, 129, 243
Seibert M., Heckman T. M., Meurer G. R., 2002, The Astronomical Journal, 124, 46
Senchyna P., et al., 2017, MNRAS, 472, 2608
Shapley A. E., Steidel C. C., Adelberger K. L., Dickinson M., Giavalisco M., Pettini M., 2001, ApJ, 562, 95
Shapley A. E., Steidel C. C., Pettini M., Adelberger K. L., 2003, ApJ, 588, 65
Shapley A. E., Steidel C. C., Pettini M., Adelberger K. L., Erb D. K., 2006, ApJ, 651, 688
Shirazi M., Brinchmann J., 2012, MNRAS, 421, 1043
Shivaei I., et al., 2015, ApJ, 815, 98
Shivaei I., et al., 2018, ApJ, 855, 42
Shivaei I., et al., 2020, ApJ, 899, 117
Siana B., et al., 2007, ApJ, 668, 62
Skelton R. E., et al., 2014, The Astrophysical Journal Supplement Series, 214, 24
Smith L. J., Norris R. P. F., Crowther P. A., 2002, MNRAS, 337, 1309
Smith N., Götberg Y., de Mink S. E., 2018, MNRAS, 475, 772
Smith M. V., van Zee L., Salim S., Dale D., Staudaher S., Wrock T., Maben A., 2021, MNRAS, 505, 3998
Somerville R. S., Primack J. R., 1999, MNRAS, 310, 1087
Sparre M., Hayward C. C., Feldmann R., Faucher-Giguère C.-A., Muratov A. L., Kereš D., Hopkins P. F., 2017, MNRAS, 466, 88
Springel V., 2000, MNRAS, 312, 859
Springel V., Di Matteo T., Hernquist L., 2005, MNRAS, 361, 776
Stanway E. R., Eldridge J. J., 2018, MNRAS, 479, 75
Stanway E. R., Eldridge J. J., Becker G. D., 2016, MNRAS, 456, 485

Steidel C. C., Pettini M., Adelberger K. L., 2001, ApJ, 546, 665
Steidel C. C., Shapley A. E., Pettini M., Adelberger K. L., Erb D. K., Reddy N. A., Hunt M. P., 2004, The Astrophysical Journal, 604, 534
Steidel C. C., Strom A. L., Pettini M., Rudie G. C., Reddy N. A., Trainor R. F., 2016, ApJ, 826, 159
Theios R. L., Steidel C. C., Strom A. L., Rudie G. C., Trainor R. F., Reddy N. A., 2019, The Astrophysical Journal, 871, 128
Topping M. W., Shapley A. E., Reddy N. A., Sanders R. L., Coil A. L., Kriek M., Mobasher B., Siana B., 2020, MNRAS, 495, 4430
Tremonti C. A., et al., 2004, ApJ, 613, 898
Vidal-García A., Charlot S., Bruzual G., Hubeny I., 2017, MNRAS, 470, 3532
Visbal E., Haiman Z., Bryan G. L., 2015, MNRAS, 450, 2506
Walborn N. R., Nichols-Bohlin J., Panek R. J., 1985, NASA Reference Publication, 1155
Weisz D. R., et al., 2012, ApJ, 744, 44
Wuyts S., et al., 2011, The Astrophysical Journal, 738, 106
Wuyts S., et al., 2012, The Astrophysical Journal, 753, 114
Zahid H. J., Dima G. I., Kudritzki R.-P., Kewley L. J., Geller M. J., Hwang H. S., Silverman J. D., Kashino D., 2014, ApJ, 791, 130
da Silva R. L., Fumagalli M., Krumholz M., 2012, ApJ, 745, 145
da Silva R. L., Fumagalli M., Krumholz M. R., 2014, MNRAS, 444, 3275
de Mello D. F., Schaerer D., Heldmann J., Leitherer C., 1998, ApJ, 507, 199
de Mink S. E., Langer N., Izzard R. G., Sana H., de Koter A., 2013, The Astrophysical Journal, 764, 166
van der Wel A., et al., 2014, ApJ, 792, L6

This paper has been typeset from a TEX/LATEX file prepared by the author.